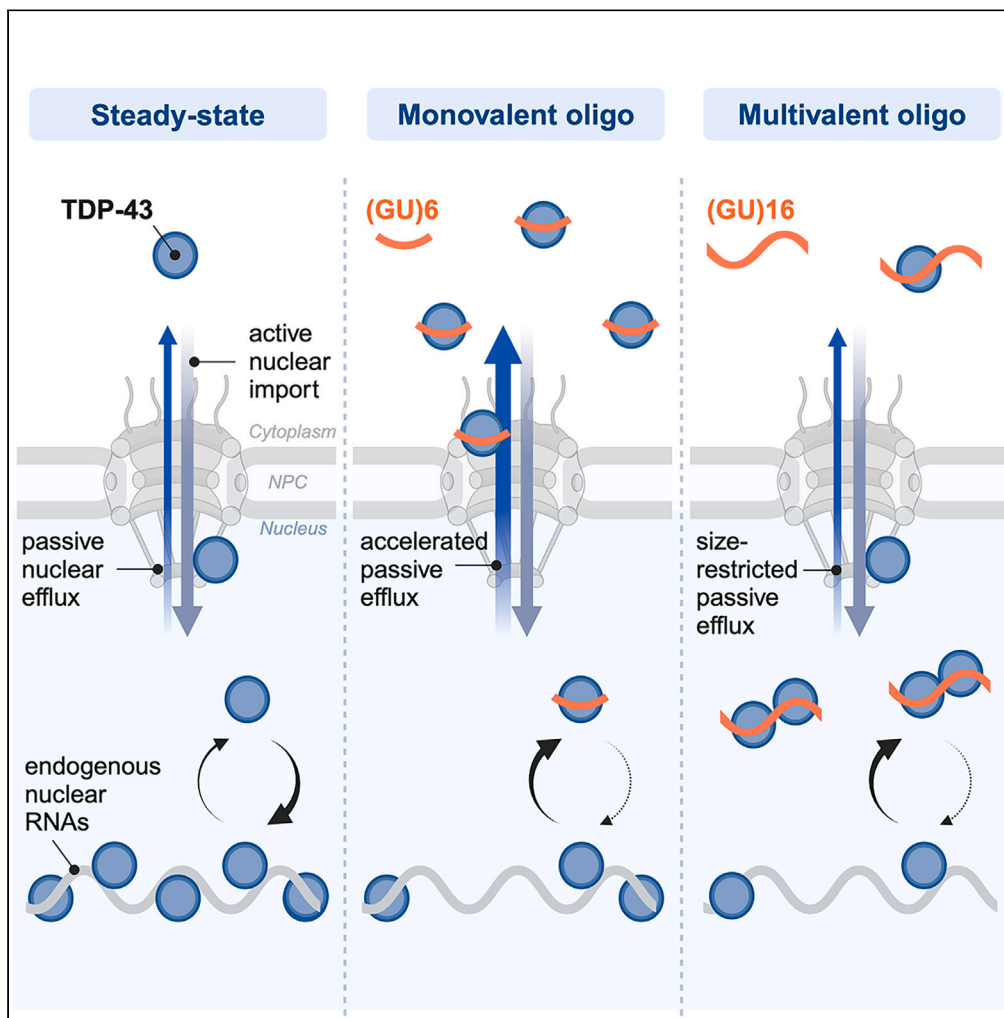CellPress
OPEN ACCESS

Article

Multivalent GU-rich oligonucleotides sequester TDP-43 in the nucleus by inducing high molecular weight RNP complexes

Xi Zhang, Tanuza Das, Tiffany F. Chao, ..., Jonathan P. Ling, Petr Kalab, Lindsey R. Hayes

petr@jhu.edu (P.K.)
lhayes@jhmi.edu (L.R.H.)

Highlights

TDP-43 binding to multivalent GU-RNA oligos induces high molecular weight complexes

Multivalent GU-RNAs promote TDP-43 nuclear localization in living cells

Pure GU-repeat oligos, but not A,C-interspersed GU motifs, disrupt TDP-43 function

CellPress

Article

Multivalent GU-rich oligonucleotides sequester TDP-43 in the nucleus by inducing high molecular weight RNP complexes

Xi Zhang,[1] Tanuza Das,[1] Tiffany F. Chao,[4] Vickie Trinh,[2] Rogger P. Carmen-Orozco,[2] Jonathan P. Ling,[3] Petr Kalab,[4,*] and Lindsey R. Hayes[1,5,6,*]

SUMMARY

TDP-43 nuclear clearance and cytoplasmic aggregation are hallmarks of TDP-43 proteinopathies. We recently demonstrated that binding to endogenous nuclear GU-rich RNAs sequesters TDP-43 in the nucleus by restricting its passive nuclear export. Here, we tested the feasibility of synthetic RNA oligonucleotide-mediated augmentation of TDP-43 nuclear localization. Using biochemical assays, we compared the ability of GU-rich oligonucleotides to engage in multivalent, RRM-dependent binding with TDP-43. When transfected into cells, (GU)16 attenuated TDP-43 mislocalization induced by transcriptional blockade or RanGAP1 ablation. Clip34nt and (GU)16 accelerated TDP-43 nuclear re-import after cytoplasmic mislocalization. RNA pulldowns confirmed that multivalent GU-oligonucleotides induced high molecular weight RNP complexes, incorporating TDP-43 and possibly other GU-binding proteins. Transfected GU-repeat oligos disrupted TDP-43 cryptic exon repression, likely by diverting TDP-43 from endogenous RNAs, except for Clip34nt that contains interspersed A and C. Thus, exogenous multivalent GU-RNAs can promote TDP-43 nuclear localization, though pure GU-repeat motifs impair TDP-43 function.

INTRODUCTION

TDP-43 is an essential nucleic acid-binding protein that regulates many aspects of RNA metabolism, including pre-mRNA splicing and stability.[1] Like other heterogeneous nuclear ribonucleoproteins (hnRNPs), TDP-43 shuttles between the nucleus and cytoplasm and is predominantly nuclear in healthy cells.[2,3] In "TDP-43 proteinopathies," a class of neurodegenerative disorders that includes amyotrophic lateral sclerosis (ALS), frontotemporal dementia (FTD), limbic-predominant age-related TDP-43 encephalopathy (LATE), and related disorders, affected cells in the central nervous system show TDP-43 nuclear clearance and cytoplasmic aggregation.[4] Though TDP-43 mutations have been identified in rare genetic cases,[5] most patients with TDP-43 proteinopathy have sporadic, non-inherited disease. Despite advances in understanding the regulation of TDP-43 nucleocytoplasmic transport and the downstream consequences of TDP-43 mislocalization,[6] the molecular events initiating TDP-43 mislocalization in neurodegeneration remain obscure. The development of therapies targeting TDP-43 nuclear clearance, loss of function, and cytoplasmic aggregation is of major interest toward slowing the progression of neurodegeneration.[7]

TDP-43 is a 43-kDa protein with an N-terminal oligomerization domain followed by a nuclear localization sequence (NLS), tandem RNA recognition motifs (RRM1 and RRM2), and a C-terminal intrinsically disordered region that mediates liquid-liquid phase separation (LLPS).[8] Structural analysis demonstrates that the RNA-binding groove of RRM1-2 contacts 10 nucleotides of a 5'-GNGUGNNUGN-3' motif, with 'AUG12' (5'-GUGUGAAUGAAU-3') binding TDP-43 stably in a single conformation.[9] Crosslinking immunoprecipitation (CLIPseq) from cell lines, mouse, and postmortem human brain confirms that TDP-43 binds GU- and G,U,A-rich RNA motifs primarily within introns, as well as a subset of noncoding RNAs, miRNAs, and mRNAs.[10–12] Notably, TDP-43 binds its own 3'-UTR at a sequence termed Clip34nt to autoregulate its expression.[10,13] Binding up to one-third of the mammalian transcriptome, TDP-43 functions prolifically in the regulation of RNA processing, including alternative splicing,[10,11] the repression of cryptic exons,[12,14,15] alternative polyadenylation,[16–20] and the processing of miRNA[21] and lncRNAs, including long interspersed nuclear elements (LINEs).[22]

The nucleocytoplasmic localization of TDP-43 is regulated by a dynamic balance between nuclear import and export. The active nuclear import of TDP-43 primarily occurs via NLS binding to importins α and β.[2,23] In addition, the recently discovered binding of importin β to the C-terminal domain of TDP-43 revealed a potential NLS-independent import pathway for TDP-43-ΔNLS.[24] Because TDP-43-ΔNLS showed only

[1]Department of Neurology, Johns Hopkins School of Medicine, Baltimore, MD 21205, USA
[2]Department of Neuroscience, Johns Hopkins School of Medicine, Baltimore, MD 21205, USA
[3]Department of Pathology, Johns Hopkins School of Medicine, Baltimore, MD 21205, USA
[4]Johns Hopkins University Whiting School of Engineering, Baltiomre, MD 21218, USA
[5]Johns Hopkins Brain Science Institute, Baltimore, MD 21205, USA
[6]Lead contact
*Correspondence: petr@jhu.edu (P.K.), lhayes@jhmi.edu (L.R.H.)

limited nuclear entry relative to wild-type TDP-43 in heterokaryon assays,[2] the NLS-independent import may be significantly slower. The nuclear export of full-length TDP-43, initially thought to occur via exportin-1 (XPO1) binding to a putative nuclear export signal (NES) in the RRM2 domain, was subsequently shown to occur by passive diffusion through nuclear pore channels and is exquisitely size-dependent.[25–28] In multiple export assays, the addition of bulky tags markedly delayed TDP-43 nuclear export by raising its size above the permeability barrier of the nuclear pore complex (NPC), which increasingly excludes cargoes above 30–60 kDa in size.[29] An exception is the short TDP-43 isoform, which is upregulated by pathologic hyperexcitability and localizes to the cytoplasm via a distinct NES for XPO1 arising in the C-terminus.[30]

We recently demonstrated that the nuclear localization of full-length TDP-43 critically depends on binding to nuclear RNAs, which sequester TDP-43 in the nucleus and restrict its availability for passive nuclear export.[28] In permeabilized and live cell nuclear export assays, depletion of nuclear RNA-binding sites for TDP-43, via RNase degradation or inhibition of transcription, released TDP-43 for passive diffusion from the nucleus. RRM mutations or displacement of TDP-43 from endogenous nuclear RNAs with monovalent (GU)6 oligonucleotides also promoted cytoplasmic mislocalization. Conversely, inhibiting splicing to promote the accumulation of nuclear intronic binding sites for TDP-43 promoted TDP-43 nuclear retention. Based on these data, we hypothesized that longer exogenous GU-rich oligonucleotides might augment TDP-43 nuclear localization, provided the oligonucleotides form multivalent complexes with TDP-43 large enough to restrict its diffusion through the NPC.

Here, we report the characterization and functional outcome of GU-rich oligonucleotides tested for their ability to promote TDP-43 nuclear retention. The TDP-43 binding valency of GU- and G,U,A-rich oligonucleotides with ≥2 predicted TDP-43-binding sites, of differing lengths and sequences, was tested in biochemical assays and living cells. (GU)16 > Clip34nt > ('AUG12')2 induced TDP-43 RRM1,2 multimerization *in vitro* and promoted the formation of heterogeneous, high molecular weight TDP-43 complexes in living cells. Remarkably, (GU)16 attenuated TDP-43 mislocalization following transcriptional blockade and RanGAP1 ablation, confirming that exogenous oligonucleotides can scaffold TDP-43 and promote its nuclear retention. Clip34nt and (GU)16 also accelerated TDP-43 nuclear re-import after cytoplasmic mislocalization. However, transfected oligos containing tandem GU-repeats caused unwanted disruption of TDP-43 cryptic exon repression, likely by diverting TDP-43 from endogenous RNAs. Clip34nt, perhaps due to its lower-affinity, A,C-interspersed sequence, largely spared TDP-43 function both by a cryptic exon reporter and at endogenous cryptic targets, indicating that further optimization of oligo motifs may enable RNA-mediated promotion of TDP-43 nuclear localization without compromising its function.

RESULTS

Multivalent interactions of GU-rich oligonucleotides with TDP-43

GU-rich oligonucleotide sequences were selected with well-characterized TDP-43-binding motifs and the established or predicted ability to form multimers with TDP-43 (Figure 1A). The multivalent binding of TDP-43 to GU-rich RNAs is well demonstrated. Endogenous TDP-43 RNA binding sites frequently occur in clusters that coordinate multivalent binding depending on sequence, length, and density.[31] Biochemical assays confirm that the valency of TDP-43 binding to synthetic (GU)n oligonucleotides is length-dependent, with monovalent binding ≤(GU)6 and multivalent binding ≥(GU)12.[32] Pure GU-repeats and the 'AUG12' motif exhibit low nanomolar affinity (0.8–26.9 nM) for TDP-43 in *in vitro* assays,[9,33–35] whereas Clip34nt affinity has been estimated at 97–520 nM.[34,36] Clip34nt is a 34-nucleotide G, U, and A-rich sequence that strongly promotes TDP-43 LLPS[33] and has shown promise as a chaperone to disaggregate cytoplasmic TDP-43.[37] The Clip34nt binding valency for TDP-43 has not yet been established.

(GU)16, ('AUG12')2, and Clip34nt oligonucleotides were synthesized with 2′-O-methyl and phosphorothioate (PS)-modifications commonly utilized to stabilize antisense oligonucleotides (ASO) against RNase degradation,[38] and binding to recombinant SUMO-tagged RRM1,2 was analyzed. First, electrophoretic mobility shift assays (EMSAs) were performed by combining each oligonucleotide with increasing concentrations of RRM1,2, and RNA-protein complexes were resolved by native electrophoresis (Figures 1B and 1C). All three GU-rich oligonucleotides readily bound RRM1,2. A32 and (CA)16 were utilized as controls for specificity, and no appreciable binding with RRM1,2 was observed. As previously reported,[32] (GU)6 showed a single-band shift with increasing RRM1,2 concentrations, indicating strictly monovalent complexes. ('AUG12')2, Clip34nt, and (GU)16, all exhibited multiple, discrete band shifts with increasing protein concentrations, suggesting multimers. Quantifying band shifts likely to involve more than two RRM1,2 molecules showed that (GU)16 had the highest propensity for multivalency, followed by Clip34nt (Figure 1C). Band shifts corresponding to complexes with >2 RRM1,2 were rare for ('AUG12')2. To determine the molecular weight of the RNA-protein complexes, the amine-crosslinker bis(sulfosuccinimidyl)suberate (BS3) was utilized before SDS-PAGE, and proteins were visualized with silver stain (Figure 1D). As predicted from the EMSAs, (GU)6 formed monomers, ('AUG12')2 formed a mix of monomers and dimers, and Clip34nt and (GU)16 additionally formed ~120–130 kDa complexes, likely corresponding to tetramers of RRM1,2. The putative tetrameric complexes appeared most abundant with (GU)16 although silver stain is poorly quantitative.

Binding valency predicts the effect of GU-rich oligonucleotides on TDP-43 nuclear localization

Previously, we showed that (GU)6 rapidly entered transfected HeLa cell nuclei, bound TDP-43, and promoted nuclear efflux, likely by competitive displacement of TDP-43 from endogenous nuclear RNAs, freeing the resulting ~45 kD complex for passive diffusion through nuclear pore channels.[28] Since (GU)6 exclusively forms monovalent complexes with TDP-43 (Figures 1B and 1C), next we tested multivalent GU-oligonucleotides along with a (CA)16 control. A 3′-biotin label was utilized to enable oligonucleotide visualization and biochemical analysis. Five hours post-transfection, cells were fixed and labeled with fluorescently tagged streptavidin (SAV). (CA)16-bio, ('AUG12')2-bio, Clip34nt-bio, and (GU)16-bio readily entered transfected cells (Figure 2A). The N/C partitioning of the oligonucleotides differed, with (CA)16 and ('AUG12')2 showing nuclear enrichment and Clip34nt and (GU)16-bio showing more equivalent nuclear and cytoplasmic signal (Figure 2B). TDP-43
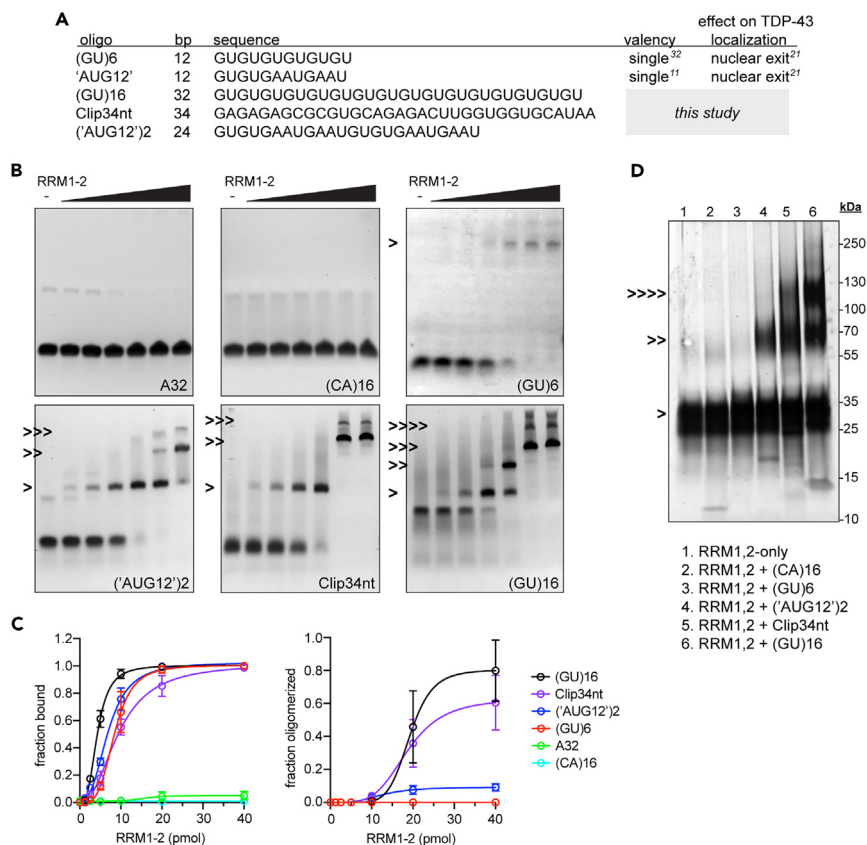
Figure 1. GU-rich oligonucleotides bind TDP-43 RRM1,2 with variable multivalency

(A) Oligonucleotide sequences tested in this study. For base modifications see Table S1.

(B) EMSA assays in which 10 pmol oligonucleotide was mixed with 0–40 pmol recombinant RRM1-2 protein, resolved under native conditions, and visualized with SYBR gold nucleic acid stain. Band shifts corresponding to predicted monomers (>), dimers (>>), trimers (>>>), or tetramers (>>>>) are indicated.

(C) Left: total bound RNA fraction from EMSA assays in (B), quantified as the sum of all shifted bands divided by the total RNA signal. Right: oligomerized RNA fraction from EMSA assays in (B), quantified as the sum of bands predicted to contain >2 RRM1,2 molecules, divided by the total RNA signal. Mean $\pm$ SD is shown for 3–6 biological replicates.

(D) BS3-crosslinked RRM1,2-oligonucleotide complexes (10 pmol oligo + 40 pmol protein) analyzed by SDS-PAGE and visualized with silver stain. Bands corresponding to predicted monomers (>), dimers (>>), and tetramers (>>>>) are indicated. Representative of three biological replicates.

immunolabeling demonstrated that ('AUG12')2, which showed the lowest propensity for multivalent binding, elicited dose-dependent TDP-43 nuclear exit (Figures 2C and 2D), reminiscent of (GU)6.[28] Clip34nt elicited modest nuclear exit. In contrast, (GU)16 did not alter the steady-state localization of TDP-43. Thus, the tendency of GU-rich oligonucleotides to elicit TDP-43 nuclear efflux inversely correlated with TDP-43 binding valency. Interestingly, (CA)16, which showed the strongest nuclear localization (Figure 2B), increased the TDP-43 N/C ratio. The absence of direct interactions with RRM1,2 in EMSA (Figures 1B and 1C) and with endogenous TDP-43 in RNA pulldowns (Figure 4A) indicate that (CA)16 affected TDP-43 nuclear localization through an indirect mechanism.

Beyond shifts in nuclear/cytoplasmic localization, oligonucleotide-transfected cells displayed variable changes in the TDP-43 distribution pattern. SAV labeling showed that, in addition to diffuse signal, all four oligonucleotides formed scattered puncta in the cytoplasm, suggesting a tendency to demix and self-associate. In ('AUG12')2- and Clip34nt-transfected cells, but not in (GU)16- or (CA)16-transfected cells, cytoplasmic TDP-43 puncta were also observed by 5 h post-transfection (Figure 2C). Next, we investigated oligonucleotide-induced alterations of nuclear TDP-43 granules (Figure S1), predicting that the formation of TDP-43-oligo RNP complexes may alter TDP-43 granule morphology. Although no apparent alterations were seen in HeLa nuclei at 20x resolution (not shown), we tested U2OS cells where we have observed that endogenous TDP-43 nuclear RNP granules are readily visualized in untreated cells (Figure S1A). By 24 h, U2OS cells transfected with GU-oligonucleotides, particularly with (GU)16 and ('AUG12')2, showed a reduction in the largest nuclear granules detectable at 20x ($\geq$0.5 μm^2, Figures S1B–S1E). To detect the suspected GU-oligo-induced increase in small nuclear granules, we imaged a subset of cells at 63X/Airyscan resolution. Indeed, (GU)16 induced a significant increase in small nuclear granules (mean area $\sim$0.1 μm^2), which doubled in number compared to mock-transfected or (CA)16-transfected cells (Figures S1F–S1H). Presumably, the formation of relatively small RNPs composed of high-affinity, multivalent TDP-43-(GU)16 complexes might be involved in both the reduction in nuclear TDP-43 granule
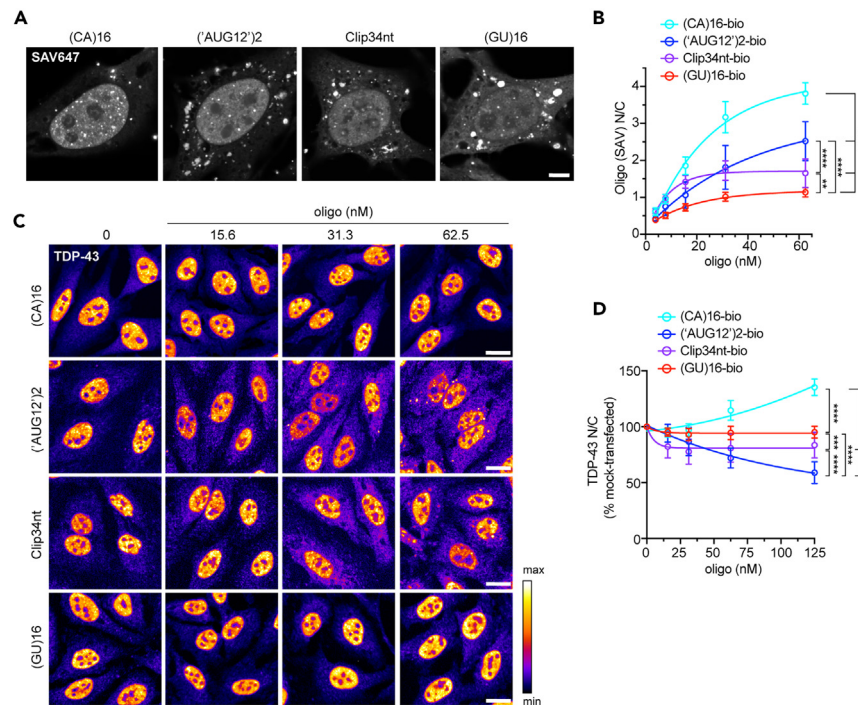
Figure 2. GU-oligonucleotide binding valency predicts the effect on TDP-43 localization in living cells

(A) Streptavidin (SAV)-647 fluorescence in HeLa cells 5 h post-transfection with biotinylated oligonucleotides (62.5 nM). Scale bar: 5 μm.

(B) SAV-647 N/C 5 h post-transfection. Mean ± SD of ≥4 biological replicates. NS = not significant; ***$p < 0.001$, ****$p < 0.0001$ by two-way ANOVA with Tukey's post-hoc test.

(C) TDP-43 immunofluorescence in oligonucleotide-transfected HeLa cells at 5 h. The intensity histogram for each image was independently spread between the dimmest and brightest pixels, and a pseudo-color linear LUT covering the full range of the data was applied (see legend). Scale bar: 20 μm. See also Figure S1.

(D) TDP-43 N/C (% untreated) in oligonucleotide-transfected HeLa cells at 5 h. Mean ± SD of ≥8 biological replicates. ***$p < 0.001$, ****$p < 0.0001$ by two-way ANOVA with Tukey's post-hoc test.

size in U2OS cells (Figures S1F–S1H) and in the paucity of cytoplasmic TDP-43 foci in (GU)16-transfected HeLa cells (Figure 2C). However, the mechanism(s) responsible for these observations await future investigation.

Multivalent GU-oligonucleotides promote TDP-43 nuclear localization

Because (GU)16 showed the highest potential for multivalent TDP-43 interactions (Figure 1) and did not induce TDP-43 nuclear efflux (Figure 2), we predicted that the size of nuclear (GU)16-TDP-43 complexes may exceed the passive diffusion limits of nuclear pore channels. To test that hypothesis, (GU)16-transfected cells were treated with the RNA Pol II inhibitor NVP2 to block transcription and deplete the nucleus of TDP-43-binding sites within nascent pre-mRNAs. As we previously reported,[28] NVP2 rapidly induced TDP-43 cytoplasmic mislocalization in untransfected cells (Figures 3A–3C). Remarkably, NVP2-induced TDP-43 mislocalization was attenuated in (GU)16-transfected cells in a dose-dependent manner. At 62.5 nM (GU)16, NVP2-induced TDP-43 nuclear efflux was completely abolished. Specifically, (GU)16 attenuated the decrease in nuclear intensity and increase in cytoplasmic intensity induced by NVP2, confirming the blockade of TDP-43 translocation to the cytoplasm (Figure S2A). In contrast, NVP2-induced TDP-43 cytoplasmic mislocalization was essentially unaltered in Clip34nt- and ('AUG12')2-transfected cells (Figures 3D and 3E). Unexpectedly, though consistent with its effect in non-NVP2-treated cells (Figures 2C and 2D), 62.5 nM (CA)16 partially attenuated NVP2-induced TDP-43 mislocalization (Figure 3F). Further investigation of the indirect mechanism for (CA)16-induced TDP-43 nuclear localization is ongoing.

To investigate (GU)16-mediated attenuation of TDP-43 mislocalization from other perturbations, we tested the acute ablation of RanGAP1, the Ran GTPase-activating protein, which has been implicated in nucleocytoplasmic transport defects in mutant *C9ORF72* and TDP-43 aggregation models (Figure S3).[39,40] DLD1 cells containing an auxin-inducible degron (AID) integrated at the endogenous RanGAP1 locus and TIR1 ligase inserted at the C-terminus of RCC1 via a self-cleavable P2A sequence were generously provided by the Dasso lab.[41] Auxin drives the rapid TIR1-dependent ubiquitination and degradation of RanGAP1 in this cell line within 2 h (Figures S3A and S3B), accompanied by severe TDP-43 cytoplasmic mislocalization (Figure S3B). Compared to mock-transfected cells, RanGAP1-AID cells transfected with (GU)16 for 5 h prior to auxin treatment showed dose-dependent attenuation of TDP-43 mislocalization (Figures S3C and S3D). The effect was modest compared to NVP2, in part due to poor transfection efficiency of the DLD1 cells, which showed only ∼25%–30% (GU)16 nuclear uptake
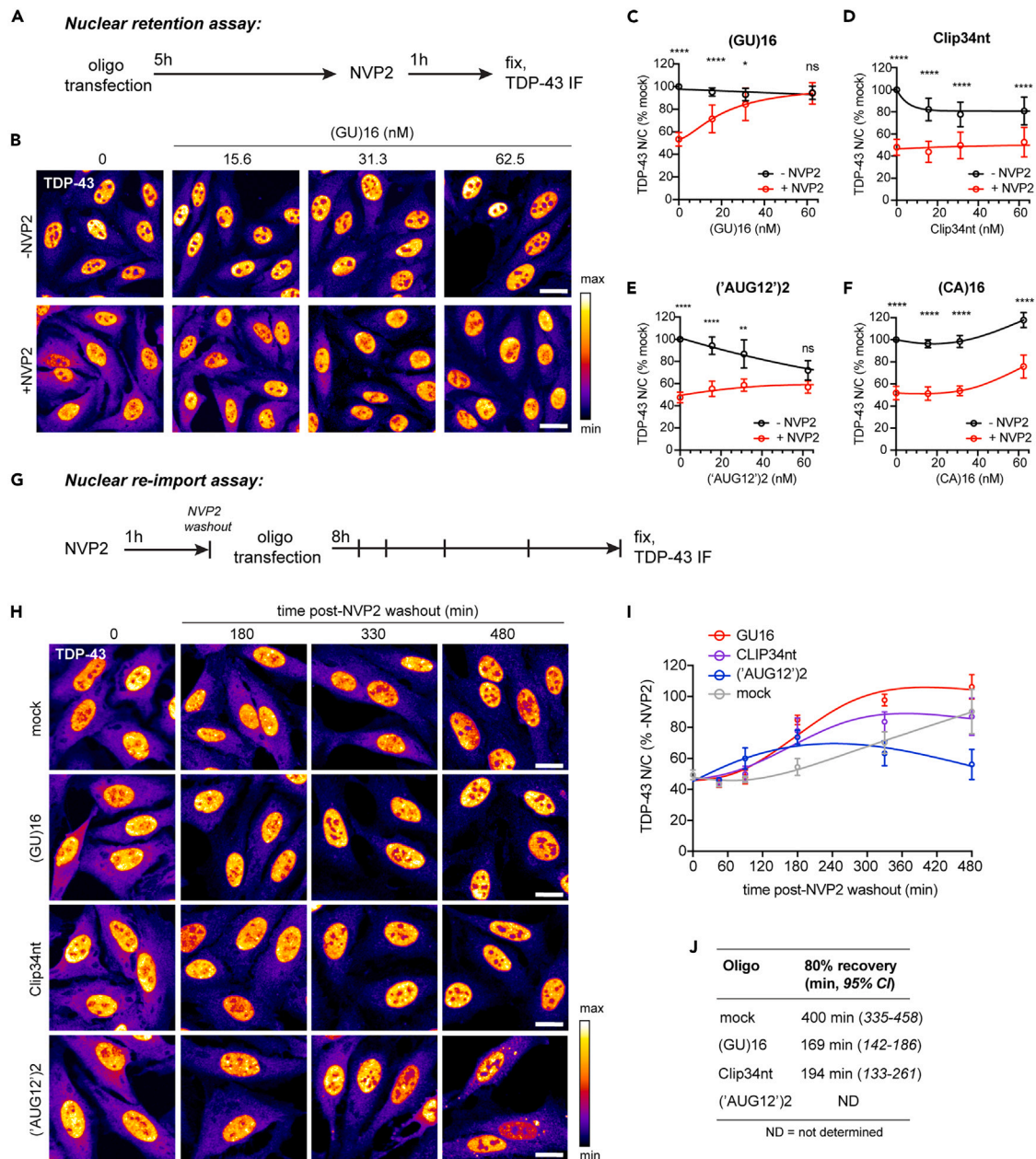
Figure 3. Multivalent GU-oligonucleotides attenuate transcriptional-blockade-induced TDP-43 mislocalization and accelerate nuclear re-import

(A) Schematic of the nuclear retention assay, in which oligonucleotides were first transfected into HeLa cells, incubated for 5 h, and TDP-43 mislocalization induced by NVP2 transcriptional blockade (250 nM for 1 h), prior to fixation and TDP-43 immunostaining.

(B) Representative TDP-43 immunofluorescence images, nuclear retention assay. Scale bar: 20 μm.

(C–F) TDP-43 N/C (% mock-transfected cells, i.e., Lipofectamine only) in (GU)16- (C), Clip34nt- (D), ('AUG12')2- (E), or (CA)16 (F)-transfected cells with or without NVP2 treatment. Mean ± SD of ≥7 biological replicates. Note: -NVP2 curves are the same as in Figure 2D. See also Figures S2 and S3.

(G) Schematic of the nuclear re-import assay, in which TDP-43 mislocalization was first induced by NVP2 treatment (250 nM for 1 h), followed by NVP2 washout and oligonucleotide transfection. A subset of cells were fixed immediately after NVP2 treatment and at time points up to 8 h for TDP-43 immunostaining.

(H) Representative TDP-43 immunofluorescence images, nuclear re-import assay. Scale bar: 20 μm.

(I) TDP-43 N/C normalized non-NVP2-treated cells at each time point. Mean ± SD of three biological replicates.

(J) Non-linear regression analysis of time to 80% recovery (minutes); 95% confidence intervals are shown.

In (B, H) the intensity histogram for each image was independently spread between the dimmest and brightest pixels, and a pseudo-color linear LUT covering the full range of the data was applied (see legend).

In (C–F) NS = not significant; *$p < 0.05$, **$p < 0.01$, ***$p < 0.001$, ****$p < 0.0001$ by two-way ANOVA with Tukey's post-hoc test.

compared to HeLa cells (Figure S3E). Additionally, RanGAP1 ablation likely inhibits Ran-regulated nucleocytoplasmic transport, including TDP-43 nuclear re-import, which is not affected in the NVP2 assays.

Having observed that (GU)16 promotes TDP-43 nuclear retention when introduced prior to TDP-43 mislocalization, next we tested the ability of GU-oligonucleotides to promote recovery after TDP-43 mislocalization (Figure 3G). We reasoned that the recovery of TDP-43 nuclear localization after a pulse of NVP2 likely depends on the resumption of nascent RNA synthesis to repopulate nuclear TDP-43 RNA-binding sites, combined with continuous Ran- and importin-dependent nuclear import. Thus, the return of TDP-43 to the nucleus might be accelerated by the addition of exogenous, multivalent GU-RNAs. Cells were treated with NVP2 for 1 h to mislocalize TDP-43 to the cytoplasm, followed by NVP2 washout and oligonucleotide transfection. Cells were fixed/immunostained for TDP-43 at multiple timepoints up to 8 h post-transfection to analyze the recovery of nuclear TDP-43 localization. Biotinylated oligos rapidly entered transfected cell nuclei at similar rates (Figures S2B and S2C). Compared to mock-transfected cells, both (GU)16 and Clip34nt significantly accelerated the recovery of nuclear TDP-43 localization (time to 80% recovery [95% CI]: 169 [142–186] and 194 [133–261] min, versus 400 [335–458] min, respectively), whereas ('AUG12') 2-transfected cells failed to recover and showed persistent cytoplasmic mislocalization (Figures 3H–3J). These findings suggest that even after depletion of endogenous nuclear pre-mRNAs, mislocalized TDP-43 that is reimported into the nucleus can be retained via binding to exogenous GU-oligos. Moreover, although substantial (GU)16 and Clip34nt is also found in the cytoplasm (Figure 2A), any cytoplasmic oligo-TDP-43 binding does not inhibit the nuclear import of TDP-43, further supported by the lack of importin β in crosslinked RNA pulldown assays (Figure S4A).

GU-oligos induce the formation of heterogeneous high molecular weight RNP complexes

Next, we tested if transfected GU-oligonucleotides induce high molecular weight RNP complexes in cells, consistent with our biochemical data (Figure 1) and the predicted mechanism of TDP-43 nuclear retention by multivalent binding. HeLa cells were transfected with biotinylated oligonucleotides. After 5 h, transfected cells were UV-irradiated to form covalent RNA-protein complexes and analyzed by SAV RNA pulldowns (Figure 4A). Only trace TDP-43 binding to (CA)16 was observed. As we previously reported, in (GU)6-transfected cells, SAV precipitated predominantly 43–45 kDa TDP-43 monomers,[28] whereas in (GU)16-transfected cells, SAV precipitated numerous higher molecular weight bands that were not multiples of 43 kD. Clip34nt and ('AUG12')2 produced similar findings, although at slightly shifted molecular weights, likely as a result of the different sizes of the crosslinked oligos. Thus, longer GU-oligos may induce the formation of heterogeneous TDP-43-containing RNP complexes that incorporate other nuclear proteins. Immunolabeling for other RNA-binding proteins (RBPs) in (GU)16-transfected cells showed that the localization of MATR3, FUS, and hnRNPL at steady state and after NVP2 treatment were unaffected by (GU)16 (Figures 4F–4H). However, (GU)16 partially attenuated the NVP2-induced nuclear efflux of hnRNPA1 and hnRNPA2/B1 (Figures 4B–4E). Neither hnRNPA1 nor hnRNPA2/B1 are predicted to bind GU-rich motifs,[42,43] but both have been shown to interact with TDP-43,[44] suggesting that the (GU)16 response may be mediated by protein-protein interactions. Consistent with this, hnRNPA1 and hnRNPA2/B1 were not identified as direct (GU)16 binders in the SAV RNA pulldowns, nor other RBPs, including MATR3, ELAVL1, ELAVL3, hnRNPC, SNRPA, or PSF (Figure S4B). hnRNPL bound (CA)16, but not (GU)16, consistent with its preferred binding to CA-repeat motifs[45] and supporting the sensitivity and specificity of the pulldowns. FUS exhibited modest, monomeric binding to (GU)16, which is not expected from its consensus motif (CAGGACAGCCAG),[46] and was insufficient to promote FUS nuclear retention (Figure 4G). Like TDP-43, the nuclear export of FUS is independent of XPO1 and likely occurs by passive diffusion.[26] We and others have found that FUS nuclear localization depends on the abundance of nuclear transcripts.[28,47] Presumably, the reason for the lack of (GU)16-induced FUS nuclear retention is the low-level and strictly monovalent binding, which is not expected to prevent the (GU)16-FUS complexes from exiting nuclei by passive diffusion through NPCs.[45]

(GU)16-induced TDP-43 nuclear retention is RRM1,2-dependent

While effective in promoting RNase resistance, PS modification of RNA oligonucleotides has also been shown to increase protein binding.[48] To verify that (GU)16-induced TDP-43 nuclear retention is mediated by specific binding to the TDP-43 RRM domains, we generated stable, monoclonal HeLa cell lines expressing V5-tagged wild-type TDP-43 (TDP43[WT]-V5) or TDP-43 containing five point mutations in the RRM1-2 domains that abolish RNA binding (TDP43[5FL]-V5)[49] (Figures 5A–5D). As we previously reported, the steady-state N/C ratio of TDP43[5FL]-V5 was reduced compared to TDP43[WT]-V5, and TDP43[5FL]-V5 showed no NVP2-induced nuclear efflux.[28] Next, the cell lines were transfected with (GU)16 for 5 h followed by NVP2 transcriptional blockade, and the localization of V5-tagged TDP-43 was analyzed by immunofluorescence. Like endogenous TDP-43 (Figure 3), (GU)16 inhibited NVP2-induced TDP43[WT]-V5 mislocalization in a dose-dependent manner (Figures 5A and 5B). However, (GU)16 had no effect on the localization of TDP43[5FL]-V5 (Figures 5C and 5D), consistent with the notion that (GU)16 alters TDP-43 localization via specific binding to the RRM1,2 domain. Pertinent to the observation of (GU)16-induced alteration of TDP-43 nuclear granule morphology, TDP43-RRM mutant constructs have been reported to form nuclear bodies or anisosomes,[50–52] which we also observed in transiently transfected cells, though as we previously reported the frequency of cells containing TDP43-RRM mutant nuclear bodies is markedly higher in TDP43[5FL]-YFP expressing cells (~100%) versus cells transiently expressing TDP43[5FL]-V5 (~12%), suggesting a contribution of the YFP tag.[28] The monoclonal TDP43[5FL]-V5 stable cell line generated here displays only rare nuclear bodies (<1% of cells, not shown) and thus is not suitable for analysis of potential effects of GU-oligo transfection on TDP43-RRM mutant nuclear bodies.

To further validate the direct (GU)16 interaction with RRM1,2, we performed SAV pulldowns from oligo-transfected TDP43[WT]-V5 or TDP43[5FL]-V5 cell lines (Figure 5E). Immunoblots of the pulldowns developed with V5 antibodies (Figure 5E, left) showed that transfection with (GU)6 and (GU)16 induced high molecular weight TDP43[WT]-V5 crosslinks, whose pattern was virtually identical to the crosslinks with endogenous TDP-43 (Figure 5E, right), except for the small increase in size resulting from the 1.4 kDa V5 tag. A barely detectable interaction
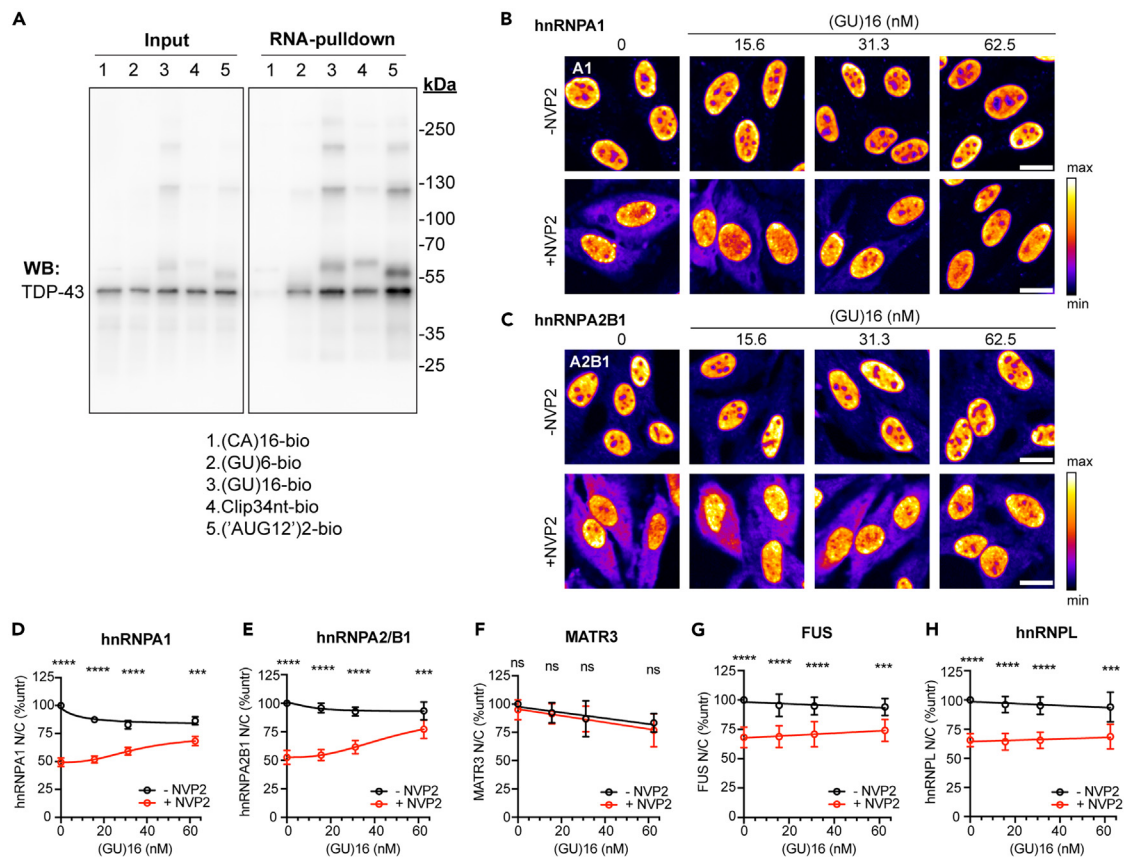
Figure 4. Formation of high molecular weight oligo-TDP-43 complexes in transfected cells

(A) SAV-RNA pulldowns in biotinylated oligo-transfected cells that were UV crosslinked before lysis and probed with rabbit anti-TDP-43. Results are representative of ≥3 biological replicates. See also Figure S4.

(B and C) hnRNPA1 (B) and hnRNPA2B1 (C) immunofluorescence in cells transfected with (GU)16 for 5 h followed by 1 h transcriptional blockade with NVP2 (250 nM). The intensity histogram for each image was independently spread between the dimmest and brightest pixels, and a pseudo-color linear LUT covering the full range of the data was applied (see legend). Scale bar: 20 μm.

(D–H) N/C ratio of hnRNPA1 (D), hnRNPA2B1 (E), Matrin-3 (F), FUS (G), and hnRNPL (H) in cells transfected with (GU)16 for 5 h followed by 1 h with or without NVP2 treatment. Mean ± SD of ≥4 biological replicates is shown. NS = not significant, ***$p < 0.001$, ****$p < 0.0001$ by two-way ANOVA with Tukey's post-hoc test.

of TDP43[5FL]-V5 with (GU)16 was noted (Figure 5E, left). TDP43[WT]-V5, but not TDP43[5FL]-V5, showed trace binding to (CA)16. As previously demonstrated,[36] TDP43[WT]-V5, but not TDP43[5FL]-V5, downregulated endogenous TDP-43 expression via autoregulation (Figure 5E, inset).[36] These data confirm that (GU)16 regulates TDP-43 localization by specific direct binding to the RRM1,2 domains.

GU-repeat-containing oligonucleotides cause TDP-43 loss of function

GU-rich oligonucleotides exhibit low nanomolar affinity for TDP-43,[9,33–36] and PS modification increases oligonucleotide protein binding.[48] We suspected that although (GU)16 preserves steady-state TDP-43 nuclear localization (Figures 2 and 3), high-affinity binding of PS-protected (GU)16 to TDP-43 may divert TDP-43 from endogenous RNAs and disrupt TDP-43 splicing regulatory function. To test this, we analyzed TDP-43 cryptic exon repression in *EPB41L4A*, a TDP-43-regulated transcript in HeLa cells[12,15] and human neurons[53] (Figure 6). To assess *EPB41L4A* sensitivity as a TDP-43 functional readout, we first generated samples in which TDP-43 protein was depleted by approximately 50% (24 h post-siRNA transfection) versus cells in which TDP-43 was fully depleted by CRISPR (Figure 6A).[54] RT-PCR confirmed that *EPB41L4A* cryptic exon inclusion is detectable even after 50% loss of TDP-43 protein (Figure 6B). Cells transfected with (CA)16 for 6, 18, or 24 h showed no *EPB41L4A* cryptic exon inclusion, in contrast to (GU)16-transfected cells where the *EPB41L4A* cryptic exon was detectable by 6 h and increased by 18 h. To quantitatively compare TDP-43 loss of function (LOF) between oligonucleotides and account for the decrease in *EPB41L4A* mRNA with TDP-43 knockdown,[12] we designed an RT-qPCR assay to quantify *EPB41L4A* cryptic exon versus mRNA levels, normalized to an internal spike-in control (Figure 6C). Clip34nt, ('AUG12')2, and (GU)16 all disrupted *EPB41L4A* cryptic exon repression, but interestingly the Clip34nt-induced LOF was much less severe than ('AUG12')2 and (GU)16. Similar results were obtained for a cryptic exon in *ARHGAP32* (Figure 6D).[15]

To evaluate these findings in an orthogonal system, we generated an HEK293 cell line stably expressing a bichromatic splicing reporter based on a TDP-43-regulated cryptic exon in mouse *Adnp2* (Figure 6E). First, we validated that siRNA knockdown of TDP-43 induced a shift in
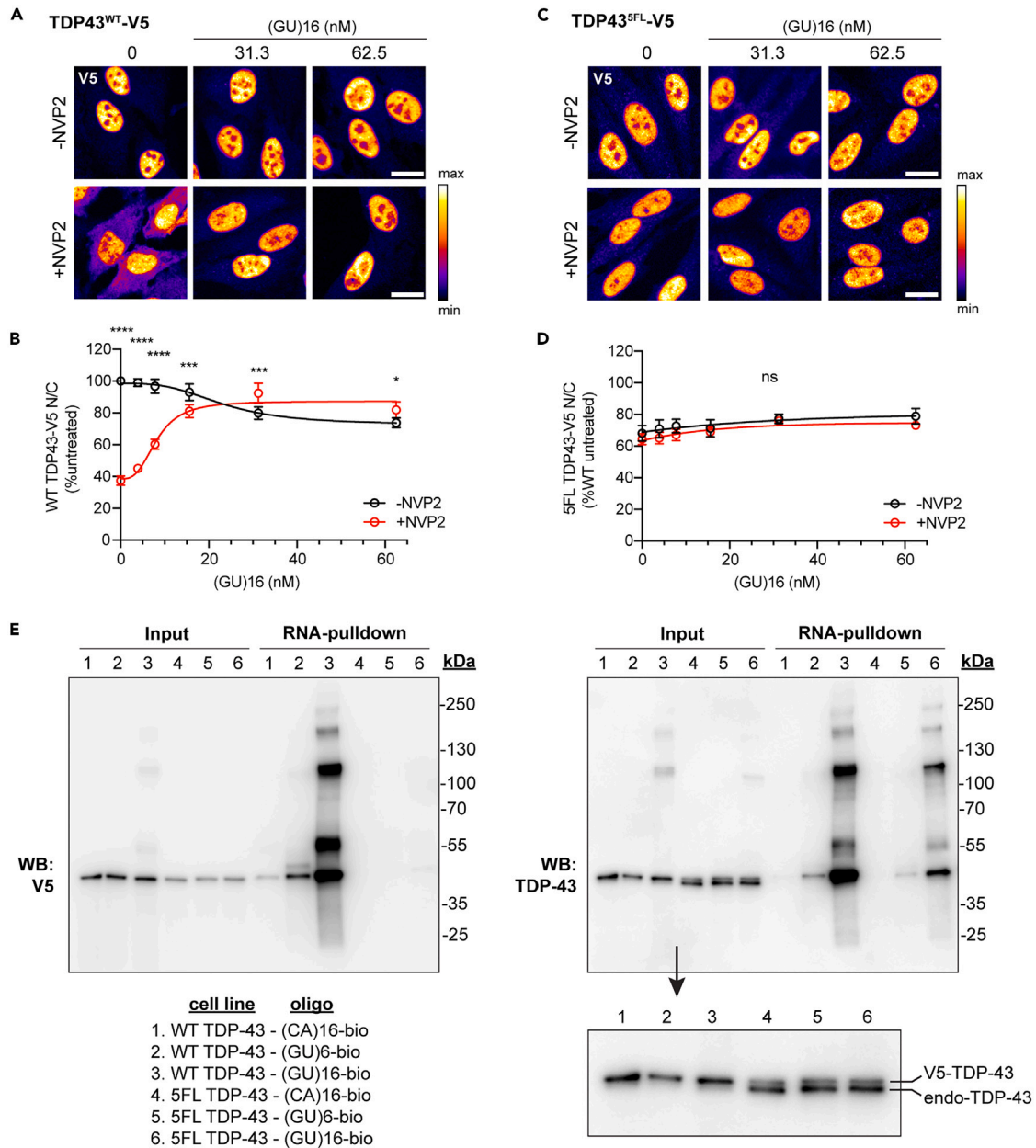
Figure 5. TDP-43 binding to (GU)16 is RRM1,2-dependent

(A and B) V5 immunofluorescence (A) and N/C ratio (B) from TDP43WT-V5 monoclonal HeLa cells transfected with (GU)16 for 5 h, +/− subsequent 1 h NVP2 treatment.

(C and D) V5 immunofluorescence (C) and N/C ratio (D) from TDP435FL-V5 monoclonal HeLa cells transfected with (GU)16 for 5 h, with or without subsequent NVP2 treatment.

(E) SAV-RNA pulldowns from biotinylated oligo-transfected cells that were UV crosslinked before lysis and probed with mouse anti-V5 (left) or rabbit anti-TDP-43 (right). Inset demonstrates ~1.4 kDa separation between V5-tagged and endogenous TDP-43 and the expected presence (TDP43WT-V5 cells, lanes 1–3) or absence (TDP435FL-V5 cells, lanes 4–6) of TDP-43 autoregulation.

In (A, C), the intensity histogram for each image was independently spread between the dimmest and brightest pixels and a pseudo-color linear LUT covering the full range of the data was applied (see legend). Scale bar: 20 μm.

In (B, D), N/C is expressed as % mock transfected cells. Mean ± SD of four biological replicates is shown. NS = not significant; *$p < 0.05$, ***$p < 0.001$, ****$p < 0.0001$ by two-way ANOVA with Tukey's post-hoc test.
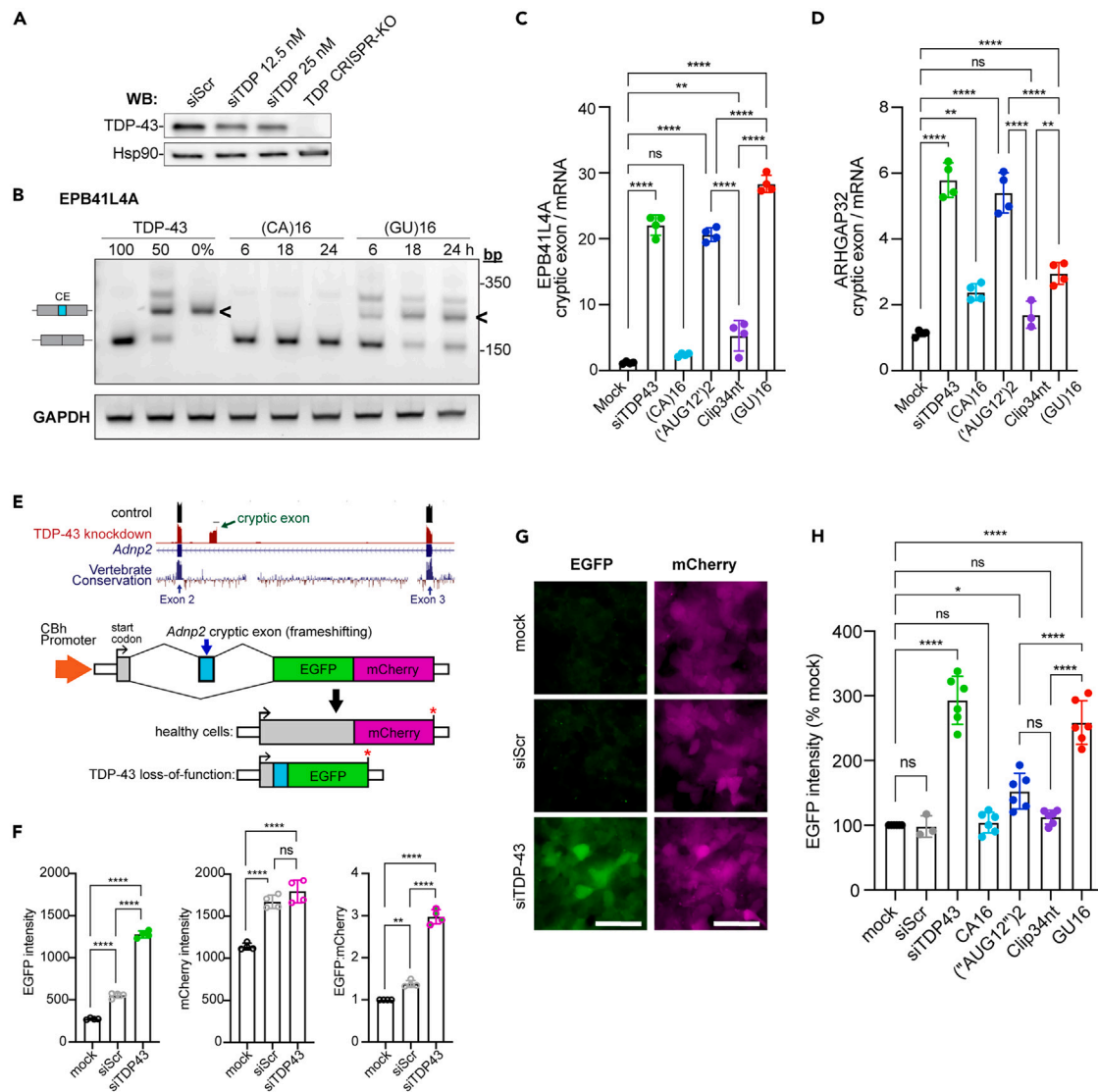
Figure 6. GU-repeat oligonucleotides disrupt TDP-43 function in cryptic exon repression

(A) TDP-43 immunoblot 24 h post-transfection with scrambled siRNA (siScr) or 12.5–25 nM TDP-43 siRNA (siTDP), compared to a stable TDP-43 CRISPR knockout (KO) cell line. Hsp90 is used as a loading control.

(B) RT-qPCR of *EPB41L4A* cryptic exon (CE <) inclusion in (CA)16 vs. (GU)16-transfected cells at 6, 18, and 24 h post-transfection. Controls for TDP-43 expression level include untreated cells (100%), TDP-43 siRNA-treated cells, 24 h (50%), and TDP-43 CRISPR knockout cells (0%). Representative of >3 biological replicates. For primers, see Table S2.

(C) RT-qPCR of *EPB41L4A* cryptic exon inclusion in oligonucleotide-transfected cells, expressed as a ratio of cryptic exon to *EPB41L4A* mRNA. TDP-43 expression controls are as in (A and B). Mean ± SD of *n* = 4 biological replicates.

(D) RT-qPCR of *ARHGAP32* cryptic exon inclusion in oligonucleotide-transfected cells, expressed as a ratio of cryptic exon to *ARHGAP32* mRNA. TDP-43 expression controls are as in (A and B). Mean ± SD of *n* = 4 biological replicates. A single outlier was removed from Clip34nt (7.6) via Grubbs test (α = 0.05).

(E) Schematic of bichromatic cryptic exon reporter, utilizing the TDP-43 cryptic exon from mouse *Adnp2*, in which TDP-43 knockdown induces a shift from mCherry to EGFP expression.

(F) EGFP intensity, mCherry intensity, and EGFP:mCherry ratio in a stable HEK293 reporter cell line that was mock transfected vs. scrambled siRNA (siScr) or TDP-43 siRNA (siTDP43) and imaged at 48 h. Mean ± SD of *n* = 4 biological replicates.

(G) Representative widefield epifluorescence images of cells analyzed in (F). The intensity histogram for all images was normalized to the min/max pixel intensity in the siTDP-43 condition. Scale bar: 50 μm.

(H) EGFP intensity of cryptic exon reporter cells 24 h post-transfection with siScr, siTDP43, or the indicated oligonucleotides (62.5 nM). Mean ± SD of *n* = 6 biological replicates.

In (C, D, F, H), ns = not significant; *$p < 0.05$, **$p < 0.01$, ****$p < 0.001$ by one-way ANOVA with Tukey's post-hoc test.

fluorescence from mCherry to EGFP by live cell imaging (Figures 6F and 6G). Indeed, compared to mock-transfected or scrambled siRNA (siScr)-transfected cells, siTDP-43 transfection induced a significant increase in EGFP intensity by 48 h. At this time point, mCherry intensity had not yet decreased; rather, there was a modest non-specific increase in both siScr and siTDP-43-transfected cells, suggesting that the induction of EGFP expression is the most sensitive and specific marker of TDP-43 LOF in this cell line. Finally, we transfected the reporter cells with the RNA oligos and measured EGFP intensity at 24 h (Figure 6H). Consistent with data from endogenous cryptic exons, ('AUG12')2 and (GU)16 both induced a significant increase in EGFP intensity, whereas (CA)16 and Clip34nt had no effect. Together, these data suggest that GU-oligo-induced TDP-43 LOF may depend on sequence, with pure GU-repeat-containing motifs causing greater LOF than A,C-interspersed, G,U-rich sequences. Further systematic testing is needed.

DISCUSSION

We recently reported that TDP-43 is sequestered in the nucleus of healthy cells by binding to endogenous nuclear GU-rich RNAs, thus restricting its passive nuclear efflux.[28] In that study, we found that competitive displacement of TDP-43 from endogenous nuclear RNAs by monovalent (GU)6 freed TDP-43 for passive diffusion from the nucleus. Here, we report that multivalent (GU)16 oligonucleotides sequester TDP-43 within the nucleus by forming high molecular weight RNP complexes that exceed the passive limits of the NPC. Transfection with low nanomolar (GU)16 prevented transcriptional blockade-induced TDP-43 mislocalization and attenuated TDP-43 mislocalization due to RanGAP1 ablation. Moreover, (GU)16 and Clip34nt accelerated TDP-43 re-import after cytoplasmic mislocalization. These data further support a reaction-diffusion model of RNA-based nuclear retention of TDP-43[28] and provide proof of principle that exogenous GU-RNAs can promote TDP-43 nuclear localization. Disruption of TDP-43 function induced by oligonucleotides with pure GU-repeats was largely absent in cells transfected with interspersed Clip34nt, suggesting that future sequence optimization could lead to RNAs that support both TDP-43 nuclear localization and function.

RNA sequence-specific drivers of multivalent TDP-43 RNPs

As previously reported,[32,55] biochemical assays showed that longer GU-oligonucleotides promoted multivalent TDP-43 binding, compared to monovalent (GU)6 (Figure 1). Both native EMSA assays and BS3 cross-linking-SDS-PAGE demonstrated stronger TDP-43 RRM1,2 multimerization for 34-nt Clip34nt and 36-nt (GU)16 compared to 24-nt ('AUG12')2. The RNA length-dependent formation of multivalent TDP-43-RNA complexes depends on RRM1,2-mediated intramolecular cooperativity during binding to target RNA.[32] Although binding affinity was not measured in the current study, past studies demonstrate a higher affinity for pure GU-repeats than interspersed sequences,[9,33–36] which could also contribute to the increased multivalency that we observed for (GU)16. Indeed, a prior report found a 50-fold increase in binding affinity for Clip34nt-(GU)6 compared to Clip34nt,[34] which lacks any GU tandem repeats. RNA secondary structure may also play a role, since Clip34nt is predicted to form a hairpin, while (GU)16 and ('AUG12')2 are unstructured. The potential effect of RNA secondary structure on TDP-43-RNA binding is yet unexplored.

Oligonucleotide-induced regulation of TDP-43 localization in living cells

Upon oligonucleotide transfection into cells, additional factors likely contribute to the overall effect on TDP-43 binding and localization. Competition for oligo binding between TDP-43 and other RBPs with a similar motif preference presumably contributes to motif-specific differences in cells that is difficult to predict from biochemical assays, including differences in the localization of the oligonucleotides (Figures 2A and 2B). Surprisingly, oligo localization within cells did not predict the effect on TDP-43 nucleocytoplasmic localization and was inversely correlated, with ('AUG12')2 being the most nuclear and (GU)16 being equally distributed between the nucleus and cytoplasm. Future proteomic analysis could enable the identification of nuclear vs. cytoplasmic oligo-bound proteins in transfected cells. The dose-dependency of oligo-induced effects (Figures 3 and S3) suggests that the intracellular concentration of the oligos must reach a critical level, likely approaching the concentration of TDP-43, to alter its localization. Our results indicate that lipid-mediated transfection of synthetic oligos, in principle, meets such a requirement. Though only nanomolar concentrations were introduced, the transfection liposomes might intracellularly concentrate the oligos beyond what was added to the transfection mix, enabling successful oligo competition for nuclear TDP-43 binding.

TDP-43 LLPS regulates the native size of TDP-43 nuclear RNP complexes, which in turn dictates TDP-43 nucleocytoplasmic localization.[56] Since GU-RNA modulates TDP-43 LLPS in a length- and motif-dependent manner,[33,55] the observed GU-oligo-induced effects on TDP-43 localization (and function, discussed later) may be influenced by changes in TDP-43 LLPS. RNA motifs containing pure GU repeats differ in their ability to promote TDP-43 phase transition compared to GU intermixed with A and C.[55] Indeed, image analysis of oligo-induced changes in nuclear TDP-43 granules, likely composed of numerous TDP-43 RNPs, showed marked differences between oligos containing pure GU-repeats ((GU)16 and ('AUG12')2) versus the intermixed sequence of Clip34nt (Figure S1). Namely, ('AUG12')2 and (GU)16 induced an increase in TDP-43 nuclear granule number while reducing mean granule size. We suspect that although both oligos induced the formation of multivalent, heterogeneous, TDP-43-containing RNP complexes (Figure 4A), these RNPs are likely much smaller than TDP-43 RNPs involving endogenous RNAs,[31] which induce cooperative TDP-43 binding and the formation of very large (>700–2000 kD) RNP complexes.[56,57] Future studies utilizing size-exclusion chromatography could enable measurement of the native size of the GU-oligo-induced granules for correlation with effects on TDP-43 localization.

Differential LLPS dynamics, together with binding affinity and RBP competition, may account for the variability we observed between (GU)16 and Clip34nt in the nuclear retention and nuclear reimport assays (Figure 3). When introduced prior to transcriptional blockade (Figures 3A–3F), the oligos encounter a markedly different nuclear milieu than after NVP2 treatment (Figures 3G–3J), which rapidly depletes nuclear RNAs and induces the translocation of many RBPs to the cytoplasm.[28] Whereas high-affinity (GU)16 promoted TDP-43 localization in

both paradigms, Clip34nt only showed efficacy in the re-import assay, suggesting that the nuclear RNA- and RBP-depleted conditions may enable more optimal Clip34nt-binding and, potentially, modulation of TDP-43 LLPS. Our findings are reminiscent of biochemical studies in which, unlike A(GU)18, Clip34nt-induced TDP-43 LLPS effects were blunted in cell lysates compared to purified assays.[33] Future dedicated LLPS assays and cross-linking RNA pulldowns from the re-import assay could aid in determining if improved Clip34nt efficacy corresponds to more potent induction of high molecular weight TDP-43 RNP complexes in the re-import assay.

TDP-43 functional disruption

The observation that transfected oligos disrupt TDP-43 function (Figure 6) is predicted by the presumed mechanism of action, whereby GU-rich oligos competitively displace TDP-43 from endogenous pre-mRNA-binding sites and promote the formation of "artificial" RNP complexes. The high affinity, near-irreversible binding of PS-modified GU-oligos to TDP-43 may be the primary driver of TDP-43 LOF, since the extent of cryptic exon derepression correlated with predicted oligo affinity ((GU)16 > ('AUG12')2 ≫ Clip34nt). However, other factors may contribute. For example, ('AUG12')2 also drives substantial TDP-43 cytoplasmic mislocalization, thus depleting the nuclear pool of TDP-43. As discussed earlier, shifts in TDP-43 nuclear granule morphology (Figure S1) suggest potential oligo-induced modulation of TDP-43 LLPS, which differs by oligo length and sequence. TDP-43 LLPS regulates its splicing function by promoting condensation at a subset of RNA regulatory sites characterized by specific lengths and RNA motifs.[31] Thus, oligo-induced alterations in TDP-43 phase condensation may produce target-specific alterations in function across the transcriptome, which could be further analyzed by RNA sequencing. The finding that Clip34nt—an interspersed, non-GU-repeat sequence derived from an endogenous TDP-43-binding site—largely spared TDP-43 function suggests that screening similar endogenous motifs from CLIPseq datasets may yield additional oligonucleotides to promote TDP-43 nuclear localization without perturbing its function.

Limitations of the study

This study exclusively analyzed oligonucleotide transfection of dividing cell lines. Effects in dividing cells may not predict outcomes in neurons due to differences in endogenous RNA abundance, composition, and dynamics (e.g., synthesis, stability, modifications, and transport). Efforts are ongoing to overcome technical hurdles to studies in human neurons, including optimization of oligonucleotide length and base chemistry informed by antisense oligonucleotides and the generation of endogenously expressed RNAs that could overcome constraints of length, delivery, and variability in expression that limit the potential for translation. Additionally, the current study is limited to acute (5–24 h) time periods and relies on severe perturbations of RNA synthesis and nucleocytoplasmic transport intended to target the molecular regulation of TDP-43 localization but of uncertain relevance to disease. Transitioning to human neurons will facilitate longer-term studies of the chronic effects of synthetic oligonucleotides on TDP-43 localization and function, including neuron-specific TDP-43 splicing regulatory targets (e.g., STMN2,[16] UNC13A,[58] NPTX2[59]) and other disease-relevant phenotypes, including TDP-43 solubility. Clip34nt was recently reported to disaggregate TDP-43 inclusions formed by optogenetic clustering in HEK293 cells and human neurons.[37,60] Though TDP-43 solubility/disaggregation was not evaluated in the current study, together these findings highlight the potential for RNA-based mechanisms to regulate TDP-43 localization, function, and solubility, which warrants systematic analyses going forward.

STAR★METHODS

Detailed methods are provided in the online version of this paper and include the following:

- KEY RESOURCES TABLE
- RESOURCE AVAILABILITY
  - Lead contact
  - Materials availability
  - Data and code availability
- EXPERIMENTAL MODEL AND STUDY PARTICIPANT DETAILS
  - Cell lines
- METHOD DETAILS
  - Oligonucleotides
  - Oligonucleotide transfections
  - Immunofluorescence
  - Cryptic exon reporter assays
  - RNA extraction and RT-PCR
  - RRM1,2 cloning and recombinant protein production
  - EMSAs
  - Biotinylated RNA-pulldowns
- QUANTIFICATION AND STATISTICAL ANALYSIS
  - Microscopy and automated image analysis
  - Image processing for figures
  - Statistical analysis

AUTHOR CONTRIBUTIONS

Conceptualization: P.K. and L.H.; methodology: X.Z., T.D., T.C., V.T., R.C., J.L., P.K., and L.H.; investigation: X.Z., T.D., P.K., and L.H.; formal analysis: X.Z., T.C., P.K., and L.H.; visualization: X.Z., J.L., P.K., and L.H.; writing—original draft: X.Z., P.K., and L.H.; writing—review & editing: X.Z., T.D., J.L., P.K., and L.H.; supervision: J.L., P.K., and L.H.; funding acquisition: P.K. and L.H.

DECLARATION OF INTERESTS

The authors declare no competing interests.

REFERENCES

1. Prasad, A., Bharathi, V., Sivalingam, V., Girdhar, A., and Patel, B.K. (2019). Molecular Mechanisms of TDP-43 Misfolding and Pathology in Amyotrophic Lateral Sclerosis. Front. Mol. Neurosci. 12, 25. https://doi.org/10.3389/fnmol.2019.00025.

2. Ayala, Y.M., Zago, P., D'Ambrogio, A., Xu, Y.-F., Petrucelli, L., Buratti, E., and Baralle, F.E. (2008). Structural determinants of the cellular localization and shuttling of TDP-43. J. Cell Sci. 121, 3778–3785. https://doi.org/10.1242/jcs.038950.

3. Dreyfuss, G., Kim, V.N., and Kataoka, N. (2002). Messenger-RNA-binding proteins and the messages they carry. Nat. Rev. Mol. Cell Biol. 3, 195–205. https://doi.org/10.1038/nrm760.

4. de Boer, E.M.J., Orie, V.K., Williams, T., Baker, M.R., De Oliveira, H.M., Polvikoski, T., Silsby, M., Menon, P., van den Bos, M., Halliday, G.M., et al. (2021). TDP-43 proteinopathies: a new wave of neurodegenerative diseases. J. Neurol. Neurosurg. Psychiatry 92, 86–95. https://doi.org/10.1136/jnnp-2020-322983.

5. Buratti, E. (2015). Functional Significance of TDP-43 Mutations in Disease. Adv. Genet. 91, 1–53. https://doi.org/10.1016/bs.adgen.2015.07.001.

6. Tziortzouda, P., Van Den Bosch, L., and Hirth, F. (2021). Triad of TDP43 control in neurodegeneration: autoregulation, localization and aggregation. Nat. Rev. Neurosci. 22, 197–208. https://doi.org/10.1038/s41583-021-00431-1.

7. Hayes, L.R., and Kalab, P. (2022). Emerging Therapies and Novel Targets for TDP-43 Proteinopathy in ALS/FTD. Neurotherapeutics 19, 1061–1084. https://doi.org/10.1007/s13311-022-01260-5.

8. François-Moutal, L., Perez-Miller, S., Scott, D.D., Miranda, V.G., Mollasalehi, N., and Khanna, M. (2019). Structural Insights Into TDP-43 and Effects of Post-translational Modifications. Front. Mol. Neurosci. 12, 1199. https://doi.org/10.3389/fnmol.2019.00301.

9. Lukavsky, P.J., Daujotyte, D., Tollervey, J.R., Ule, J., Stuani, C., Buratti, E., Baralle, F.E., Damberger, F.F., and Allain, F.H.-T. (2013). Molecular basis of UG-rich RNA recognition by the human splicing factor TDP-43. Nat. Struct. Mol. Biol. 20, 1443–1449. https://doi.org/10.1038/nsmb.2698.

10. Polymenidou, M., Lagier-Tourenne, C., Hutt, K.R., Huelga, S.C., Moran, J., Liang, T.Y., Ling, S.-C., Sun, E., Wancewicz, E., Mazur, C., et al. (2011). Long pre-mRNA depletion and RNA missplicing contribute to neuronal vulnerability from loss of TDP-43. Nat. Neurosci. 14, 459–468. https://doi.org/10.1038/nn.2779.

11. Tollervey, J.R., Curk, T., Rogelj, B., Briese, M., Cereda, M., Kayikci, M., König, J., Hortobágyi, T., Nishimura, A.L., Zupunski, V., et al. (2011). Characterizing the RNA targets and position-dependent splicing regulation by TDP-43. Nat. Neurosci. 14, 452–458. https://doi.org/10.1038/nn.2778.

12. Ling, J.P., Pletnikova, O., Troncoso, J.C., and Wong, P.C. (2015). TDP-43 repression of nonconserved cryptic exons is compromised in ALS-FTD. Science 349, 650–655. https://doi.org/10.1126/science.aab0983.

13. Ayala, Y.M., De Conti, L., Avendaño-Vázquez, S.E., Dhir, A., Romano, M., D'Ambrogio, A., Tollervey, J., Ule, J., Baralle, M., Buratti, E., and Baralle, F.E. (2011). TDP-43 regulates its mRNA levels through a negative feedback loop. EMBO J. 30, 277–288. https://doi.org/10.1038/emboj.2010.310.

14. Humphrey, J., Emmett, W., Fratta, P., Isaacs, A.M., and Plagnol, V. (2017). Quantitative analysis of cryptic splicing associated with TDP-43 depletion. BMC Med. Genom. 10, 38. https://doi.org/10.1186/s12920-017-0274-1.

15. Tan, Q., Yalamanchili, H.K., Park, J., De Maio, A., Lu, H.-C., Wan, Y.-W., White, J.J., Bondar, V.V., Sayegh, L.S., Liu, X., et al. (2016). Extensive cryptic splicing upon loss of RBM17 and TDP43 in neurodegeneration models. Hum. Mol. Genet. 25, 5083–5093. https://doi.org/10.1093/hmg/ddw337.

16. Melamed, Z., López-Erauskin, J., Baughn, M.W., Zhang, O., Drenner, K., Sun, Y., Freyermuth, F., McMahon, M.A., Beccari, M.S., Artates, J.W., et al. (2019). Premature polyadenylation-mediated loss of stathmin-2 is a hallmark of TDP-43-dependent neurodegeneration. Nat. Neurosci. 22, 180–190. https://doi.org/10.1038/s41593-018-0293-z.

17. Bryce-Smith, S., Brown, A.-L., Mehta, P.R., Mattedi, F., Mikheenko, A., Barattucci, S., Zanovello, M., Dattilo, D., Yome, M., Hill, S.E., et al. (2024). TDP-43 loss induces extensive cryptic polyadenylation in ALS/FTD. Preprint at bioRxiv. https://doi.org/10.1101/2024.01.22.576625.

18. Zeng, Y., Lovchykova, A., Akiyama, T., Liu, C., Guo, C., Jawahar, V.M., Sianto, O., Calliari, A., Prudencio, M., Dickson, D.W., et al. (2024). TDP-43 nuclear loss in FTD/ALS causes widespread alternative polyadenylation changes. Preprint at bioRxiv. https://doi.org/10.1101/2024.01.22.575730.

19. Arnold, F.J., Cui, Y., Michels, S., Colwin, M.R., Stockford, C., Ye, W., Tam, O.H., Menon, S., Situ, W.G., Ehsani, K.C.K., et al. (2024). TDP-43 dysregulation of polyadenylation site selection is a defining feature of RNA misprocessing in ALS/FTD and related disorders. Preprint at bioRxiv. https://doi.org/10.1101/2024.01.22.576709.

20. Alessandrini, F., Wright, M., Kurosaki, T., Maquat, L.E., and Kiskinis, E. (2024).

ALS-Associated TDP-43 Dysfunction Compromises UPF1-Dependent mRNA Metabolism Pathways Including Alternative Polyadenylation and 3′UTR Length. Preprint at bioRxiv. https://doi.org/10.1101/2024.01.31.578311.

21. Kawahara, Y., and Mieda-Sato, A. (2012). TDP-43 promotes microRNA biogenesis as a component of the Drosha and Dicer complexes. Proc. Natl. Acad. Sci. USA 109, 3347–3352. https://doi.org/10.1073/pnas.1112427109.

22. Liu, E.Y., Russ, J., Cali, C.P., Phan, J.M., Amlie-Wolf, A., and Lee, E.B. (2019). Loss of Nuclear TDP-43 Is Associated with Decondensation of LINE Retrotransposons. Cell Rep. 27, 1409–1421.e6. https://doi.org/10.1016/j.celrep.2019.04.003.

23. Winton, M.J., Igaz, L.M., Wong, M.M., Kwong, L.K., Trojanowski, J.Q., and Lee, V.M.Y. (2008). Disturbance of nuclear and cytoplasmic TAR DNA-binding protein (TDP-43) induces disease-like redistribution, sequestration, and aggregate formation. J. Biol. Chem. 283, 13302–13309. https://doi.org/10.1074/jbc.m800342200.

24. Khalil, B., Chhangani, D., Wren, M.C., Smith, C.L., Lee, J.H., Li, X., Puttinger, C., Tsai, C.-W., Fortin, G., Morderer, D., et al. (2022). Nuclear import receptors are recruited by FG-nucleoporins to rescue hallmarks of TDP-43 proteinopathy. Mol. Neurodegener. 17, 80. https://doi.org/10.1186/s13024-022-00585-1.

25. Pinarbasi, E.S., Cağatay, T., Fung, H.Y.J., Li, Y.C., Chook, Y.M., and Thomas, P.J. (2018). Active nuclear import and passive nuclear export are the primary determinants of TDP-43 localization. Sci. Rep. 8, 7083. https://doi.org/10.1038/s41598-018-25008-4.

26. Ederle, H., Funk, C., Abou-Ajram, C., Hutten, S., Funk, E.B.E., Kehlenbach, R.H., Bailer, S.M., and Dormann, D. (2018). Nuclear egress of TDP-43 and FUS occurs independently of Exportin-1/CRM1. Sci. Rep. 8, 7084. https://doi.org/10.1038/s41598-018-25007-5.

27. Archbold, H.C., Jackson, K.L., Arora, A., Weskamp, K., Tank, E.M.H., Li, X., Miguez, R., Dayton, R.D., Tamir, S., Klein, R.L., and Barmada, S.J. (2018). TDP43 nuclear export and neurodegeneration in models of amyotrophic lateral sclerosis and frontotemporal dementia. Sci. Rep. 8, 4606. https://doi.org/10.1038/s41598-018-22858-w.

28. Duan, L., Zaepfel, B.L., Aksenova, V., Dasso, M., Rothstein, J.D., Kalab, P., and Hayes, L.R. (2022). Nuclear RNA binding regulates TDP-43 nuclear localization and passive nuclear export. Cell Rep. 40, 111106. https://doi.org/10.1016/j.celrep.2022.111106.

29. Timney, B.L., Raveh, B., Mironska, R., Trivedi, J.M., Kim, S.J., Russel, D., Wente, S.R., Sali, A., and Rout, M.P. (2016). Simple rules for passive diffusion through the nuclear pore complex. J. Cell Biol. 215, 57–76. https://doi.org/10.1083/jcb.201601004.

30. Weskamp, K., Tank, E.M., Miguez, R., McBride, J.P., Gómez, N.B., White, M., Lin, Z., Gonzalez, C.M., Serio, A., Sreedharan, J., and Barmada, S.J. (2020). Shortened TDP43 isoforms upregulated by neuronal hyperactivity drive TDP43 pathology in ALS. J. Clin. Invest. 130, 1139–1155. https://doi.org/10.1172/jci130988.

31. Hallegger, M., Chakrabarti, A.M., Lee, F.C.Y., Lee, B.L., Amalietti, A.G., Odeh, H.M., Copley, K.E., Rubien, J.D., Portz, B., Kuret, K., et al. (2021). TDP-43 condensation properties specify its RNA-binding and regulatory repertoire. Cell 184, 4680–4696.e22. https://doi.org/10.1016/j.cell.2021.07.018.

32. Rengifo-Gonzalez, J.C., El Hage, K., Clément, M.-J., Steiner, E., Joshi, V., Craveur, P., Durand, D., Pastré, D., and Bouhss, A. (2021). The cooperative binding of TDP-43 to GU-rich RNA repeats antagonizes TDP-43 aggregation. Elife 10, e67605. https://doi.org/10.7554/elife.67605.

33. Grese, Z.R., Bastos, A.C., Mamede, L.D., French, R.L., Miller, T.M., and Ayala, Y.M. (2021). Specific RNA interactions promote TDP-43 multivalent phase separation and maintain liquid properties. EMBO Rep. 22, e53632. https://doi.org/10.15252/embr.202153632.

34. Bhardwaj, A., Myers, M.P., Buratti, E., and Baralle, F.E. (2013). Characterizing TDP-43 interaction with its RNA targets. Nucleic Acids Res. 41, 5062–5074. https://doi.org/10.1093/nar/gkt189.

35. French, R.L., Grese, Z.R., Aligireddy, H., Dhavale, D.D., Reeb, A.N., Kedia, N., Kotzbauer, P.T., Bieschke, J., and Ayala, Y.M. (2019). Detection of TAR DNA-binding protein 43 (TDP-43) oligomers as initial intermediate species during aggregate formation. J. Biol. Chem. 294, 6696–6709. https://doi.org/10.1074/jbc.ra118.005889.

36. Koehler, L.C., Grese, Z.R., Bastos, A.C.S., Mamede, L.D., Heyduk, T., and Ayala, Y.M. (2022). TDP-43 Oligomerization and Phase Separation Properties Are Necessary for Autoregulation. Front. Neurosci. 16, 818655. https://doi.org/10.3389/fnins.2022.818655.

37. Mann, J.R., Gleixner, A.M., Mauna, J.C., Gomes, E., DeChellis-Marks, M.R., Needham, P.G., Copley, K.E., Hurtle, B., Portz, B., Pyles, N.J., et al. (2019). RNA Binding Antagonizes Neurotoxic Phase Transitions of TDP-43. Neuron 102, 321–338.e8. https://doi.org/10.1016/j.neuron.2019.01.048.

38. Khvorova, A., and Watts, J.K. (2017). The chemical evolution of oligonucleotide therapies of clinical utility. Nat. Biotechnol. 35, 238–248. https://doi.org/10.1038/nbt.3765.

39. Zhang, K., Donnelly, C.J., Haeusler, A.R., Grima, J.C., Machamer, J.B., Steinwald, P., Daley, E.L., Miller, S.J., Cunningham, K.M., Vidensky, S., et al. (2015). The C9orf72 repeat expansion disrupts nucleocytoplasmic transport. Nature 525, 56–61. https://doi.org/10.1038/nature14973.

40. Chou, C.-C., Zhang, Y., Umoh, M.E., Vaughan, S.W., Lorenzini, I., Liu, F., Sayegh, M., Donlin-Asp, P.G., Chen, Y.H., Duong, D.M., et al. (2018). TDP-43 pathology disrupts nuclear pore complexes and nucleocytoplasmic transport in ALS/FTD. Nat. Neurosci. 21, 228–239. https://doi.org/10.1038/s41593-017-0047-3.

41. Aksenova, V., Smith, A., Lee, H., Bhat, P., Esnault, C., Chen, S., Iben, J., Kaufhold, R., Yau, K.C., Echeverria, C., et al. (2020). Nucleoporin TPR is an integral component of the TREX-2 mRNA export pathway. Nat. Commun. 11, 4577. https://doi.org/10.1038/s41467-020-18266-2.

42. Wu, B., Su, S., Patil, D.P., Liu, H., Gan, J., Jaffrey, S.R., and Ma, J. (2018). Molecular basis for the specific and multivariant recognitions of RNA substrates by human hnRNP A2/B1. Nat. Commun. 9, 420. https://doi.org/10.1038/s41467-017-02770-z.

43. Jain, N., Lin, H.-C., Morgan, C.E., Harris, M.E., and Tolbert, B.S. (2017). Rules of RNA specificity of hnRNP A1 revealed by global and quantitative analysis of its affinity distribution. Proc. Natl. Acad. Sci. USA 114, 2206–2211. https://doi.org/10.1073/pnas.1616371114.

44. Freibaum, B.D., Chitta, R.K., High, A.A., and Taylor, J.P. (2010). Global analysis of TDP-43 interacting proteins reveals strong association with RNA splicing and translation machinery. J. Proteome Res. 9, 1104–1120. https://doi.org/10.1021/pr901076y.

45. Smith, S.A., Ray, D., Cook, K.B., Mallory, M.J., Hughes, T.R., and Lynch, K.W. (2013). Paralogs hnRNP L and hnRNP LL Exhibit Overlapping but Distinct RNA Binding Constraints. PLoS One 8, e80701. https://doi.org/10.1371/journal.pone.0080701.

46. Colombrita, C., Onesto, E., Megiorni, F., Pizzuti, A., Baralle, F.E., Buratti, E., Silani, V., and Ratti, A. (2012). TDP-43 and FUS RNA-binding proteins bind distinct sets of cytoplasmic messenger RNAs and differently regulate their post-transcriptional fate in motoneuron-like cells. J. Biol. Chem. 287, 15635–15647. https://doi.org/10.1074/jbc.m111.333450.

47. Tsai, Y.-L., Mu, Y.C., and Manley, J.L. (2022). Nuclear RNA transcript levels modulate nucleocytoplasmic distribution of ALS/FTD-associated protein FUS. Sci. Rep. 12, 8180. https://doi.org/10.1038/s41598-022-12098-4.

48. Crooke, S.T., Vickers, T.A., and Liang, X.H. (2020). Phosphorothioate modified oligonucleotide–protein interactions. Nucleic Acids Res. 48, 5235–5253. https://doi.org/10.1093/nar/gkaa299.

49. Buratti, E., and Baralle, F.E. (2001). Characterization and Functional Implications of the RNA Binding Properties of Nuclear Factor TDP-43, a Novel Splicing Regulator of CFTR Exon 9. J. Biol. Chem. 276, 36337–36343. https://doi.org/10.1074/jbc.m104236200.

50. Yu, H., Lu, S., Gasior, K., Singh, D., Vazquez-Sanchez, S., Tapia, O., Toprani, D., Beccari, M.S., Yates, J.R., Da Cruz, S., et al. (2021). HSP70 chaperones RNA-free TDP-43 into anisotropic intranuclear liquid spherical shells. Science 371, eabb4309. https://doi.org/10.1126/science.abb4309.

51. Elden, A.C., Kim, H.-J., Hart, M.P., Chen-Plotkin, A.S., Johnson, B.S., Fang, X., Armakola, M., Geser, F., Greene, R., Lu, M.M., et al. (2010). Ataxin-2 intermediate-length polyglutamine expansions are associated with increased risk for ALS. Nature 466, 1069–1075. https://doi.org/10.1038/nature09320.

52. Wang, C., Duan, Y., Duan, G., Wang, Q., Zhang, K., Deng, X., Qian, B., Gu, J., Ma, Z., Zhang, S., et al. (2020). Stress Induces Dynamic, Cytotoxicity-Antagonizing TDP-43 Nuclear Bodies via Paraspeckle LncRNA NEAT1-Mediated Liquid-Liquid Phase Separation. Mol. Cell 79, 443–458.e7. https://doi.org/10.1016/j.molcel.2020.06.019.

53. Klim, J.R., Williams, L.A., Limone, F., Guerra San Juan, I., Davis-Dusenbery, B.N., Mordes, D.A., Burberry, A., Steinbaugh, M.J., Gamage, K.K., Kirchner, R., et al. (2019). ALS-implicated protein TDP-43 sustains levels of STMN2, a mediator of motor neuron growth and repair. Nat. Neurosci. 22, 167–179. https://doi.org/10.1038/s41593-018-0300-4.

54. Roczniak-Ferguson, A., and Ferguson, S.M. (2019). Pleiotropic requirements for human TDP-43 in the regulation of cell and organelle homeostasis. Life Sci. Alliance 2, e201900358. https://doi.org/10.26508/lsa.201900358.

55. Miura, M., Sakaue, F., Matsuno, H., Morita, K., Yoshida, A., Hara, R.I., Nishimura, R., Nishida, Y., Yokogawa, M., Osawa, M., and Yokota, T.

(2023). TDP-43 N-terminal domain dimerisation or spatial separation by RNA binding decreases its propensity to aggregate. FEBS Lett. *597*, 1667–1676. https://doi.org/10.1002/1873-3468.14635.

56. Dos Passos, P.M., Hemamali, E.H., Mamede, L.D., Hayes, L.R., and Ayala, Y.M. (2024). RNA-mediated ribonucleoprotein assembly controls TDP-43 nuclear retention. PLoS Biol. *22*, e3002527. https://doi.org/10.1371/journal.pbio.3002527.

57. Sephton, C.F., Cenik, C., Kucukural, A., Dammer, E.B., Cenik, B., Han, Y., Dewey, C.M., Roth, F.P., Herz, J., Peng, J., et al. (2011). Identification of neuronal RNA targets of TDP-43-containing ribonucleoprotein complexes. J. Biol. Chem. *286*, 1204–1215. https://doi.org/10.1074/jbc.m110.190884.

58. Ma, X.R., Prudencio, M., Koike, Y., Vatsavayai, S.C., Kim, G., Harbinski, F., Briner, A., Rodriguez, C.M., Guo, C., Akiyama, T., et al. (2022). TDP-43 represses cryptic exon inclusion in the FTD–ALS gene UNC13A. Nature *603*, 124–130. https://doi.org/10.1038/s41586-022-04424-7.

59. Hruska-Plochan, M., Wiersma, V.I., Betz, K.M., Mallona, I., Ronchi, S., Maniecka, Z., Hock, E.-M., Tantardini, E., Laferriere, F., Sahadevan, S., et al. (2024). A model of human neural networks reveals NPTX2 pathology in ALS and FTLD. Nature *626*, 1073–1083. https://doi.org/10.1038/s41586-024-07042-7.

60. Guo, L., Mann, J.R., Mauna, J.C., Copley, K.E., Wang, H., Rubien, J.D., Odeh, H.M., Lin, J., Lee, B.L., Ganser, L., et al. (2023). Defining RNA oligonucleotides that reverse deleterious phase transitions of RNA-binding proteins with prion-like domains. Preprint at bioRxiv. https://doi.org/10.1101/2023.09.04.555754.

61. Kalab, P., Pralle, A., Isacoff, E.Y., Heald, R., and Weis, K. (2006). Analysis of a RanGTP-regulated gradient in mitotic somatic cells. Nature *440*, 697–701. https://doi.org/10.1038/nature04589.

62. Hayes, L.R., Duan, L., Vidensky, S., and Kalab, P. (2021). Nuclear Transport Assays in Permeabilized Mouse Cortical Neurons. J. Vis. Exp. *173*, e62710. https://doi.org/10.3791/62710.

63. Ling, J.P., Bygrave, A.M., Santiago, C.P., Carmen-Orozco, R.P., Trinh, V.T., Yu, M., Li, Y., Liu, Y., Bowden, K.D., Duncan, L.H., et al. (2022). Cell-specific regulation of gene expression using splicing-dependent frameshifting. Nat. Commun. *13*, 5773. https://doi.org/10.1038/s41467-022-33523-2.

64. Yang, C., Tan, W., Whittle, C., Qiu, L., Cao, L., Akbarian, S., and Xu, Z. (2010). The C-Terminal TDP-43 Fragments Have a High Aggregation Propensity and Harm Neurons by a Dominant-Negative Mechanism. PLoS One *5*, e15878. https://doi.org/10.1371/journal.pone.0015878.

STAR★METHODS

KEY RESOURCES TABLE

REAGENT or RESOURCE	SOURCE	IDENTIFIER
Antibodies		
Rabbit anti-TDP43 polyclonal (IF: 1:2000, WB 1:2000)	Proteintech	Cat# 10782-2-AP; RRID: AB_615042
Mouse anti-hnRNP A1 monoclonal (IF: 1:200, WB 1:200)	Santa Cruz Biotechnology	Cat# sc-32301; RRID: AB_627729
Mouse anti-hnRNP A2/B1 monoclonal (IF: 1:50, WB 1:200)	Santa Cruz Biotechnology	Cat# sc-53531; RRID: AB_2248245
Mouse anti-hnRNPC monoclonal (WB 1:800)	Santa Cruz Biotechnology	Cat# sc-32308; RRID: AB_627731
Mouse anti-hnRNP L monoclonal (IF: 1:100, WB 1:200)	Santa Cruz Biotechnology	Cat# sc-32317; RRID: AB_627736
Rabbit anti-ELAVL1 (HuR) polyclonal (WB 1:1300)	Proteintech	Cat# 11910-1-AP; RRID: AB_11182183
Rabbit anti-ELAVL3 (HuC) polyclonal (WB 1:1300)	Proteintech	Cat# 55047-1-AP; RRID: AB_10859256
Rabbit anti-FUS polyclonal (IF: 1:2000, WB 1:1000)	Bethyl	Cat# A300-302A; RRID: AB_309445
Rabbit anti-Matrin 3 monoclonal (IF 1:1000)	Abcam	Cat# ab151714; RRID: AB_2491618
Mouse anti-PSF monoclonal (WB 1:200)	Santa Cruz Biotechnology	Cat# sc-374502; RRID: AB_10989589
Mouse anti-SNRPA monoclonal (WB 1:200)	Santa Cruz Biotechnology	Cat# sc-101149; RRID: AB_2193721
Mouse anti-RanGAP1 monoclonal (WB 1:50)	Santa Cruz Biotechnology	Cat# sc-28322; RRID: AB_2176987
Mouse anti-importinβ1 (KPNB1) monoclonal (WB 1:1000)	Invitrogen	Cat# MA3-070; RRID: AB_2133986
Rabbit anti-V5 monoclonal (WB: 1:1000, IF 1:2000)	Cell Signaling Technology	Cat# 13202; RRID: AB_2687461
Mouse anti-HSP90 monoclonal (WB: 1:1000)	Santa Cruz Biotechnology	Cat# sc-13119; RRID: AB_675659
Goat anti-mouse IgG AF488 polyclonal (IF: 1:1000)	Invitrogen	Cat# A32723; RRID: AB_2633275
Goat anti-rabbit IgG AF488 polyclonal (IF: 1:1000)	Invitrogen	Cat# A32731; RRID: AB_2633280
Goat anti-mouse IgG AF647 polyclonal (IF: 1:1000)	Invitrogen	Cat# A32728; RRID: AB_2633277
Goat anti-rabbit IgG AF647 polyclonal (IF: 1:1000)	Invitrogen	Cat# A32733; RRID: AB_2633282
Horse anti-mouse IgG HRP-conjugated polyclonal (WB: 1:5000)	Cell Signaling Technology	Cat# 7076S; RRID: AB_330924
Goat anti-rabbit IgG HRP-conjugated polyclonal (WB: 1:5000)	Cell Signaling Technology	Cat# 7074S; RRID: AB_2099233
Bacterial and virus strains		
NEB 5-alpha *E.coli* (High efficiency)	New England Biolabs	Cat# C2987H
BL21(DE3) Competent *E. coli*	New England Biolabs	Cat# C2527H
Chemicals, peptides, and recombinant proteins		
NVP-2	Tocris Bioscience	Cat# 6535

(Continued on next page)

Continued

REAGENT or RESOURCE	SOURCE	IDENTIFIER
Auxin (3-indoleacetic acid)	Sigma-Aldrich	Cat# I2886
Dynabeads, MyOne Streptavidin C1	Thermo Fisher Scientific	Cat# 65001
Streptavidin, Alexa Fluor-647 conjugate	Thermo Fisher Scientific	Cat# S21374
Lipofectamine RNAiMAX	Thermo Fisher Scientific	Cat# 13778030
DharmaFECT 1	Dharmacon	Cat# T-2001-03
Critical commercial assays		
TDP-43 Taqman assay	Thermo Fisher Scientific	Cat# Hs00429203_gH
GAPDH Taqman assay	Thermo Fisher Scientific	Cat# Hs02786624_g1
EPB41L4A mRNA Taqman assay	Thermo Fisher Scientific	Cat# Hs00223297_m1
ARHGAP32 mRNA Taqman assay	Thermo Fisher Scientific	Cat# Hs00206951_m1
Taqman Universal RNA Spike-In RT control	ThermoFisher Scientific	Cat# A39179
Xeno™ Internal Positive Control Taqman Assay	ThermoFisher Scientific	Cat# A29765
MycoScope PCR Mycoplasma Detection Kit	Genlantis	Cat# MY01100
Experimental models: Cell lines		
HeLa cells (human)	ATCC and Kalab et al., 2006[61]	HeLa clone 61
TDP-43 CRISPR KO HeLa cells (human)	Roczniak-Ferguson & Ferguson, 2019[54]	N/A
U2OS cells (human)	ATCC	Cat# HTB-96
DLD1-wildtype cells (human)	ATCC and Aksenova et al., 2020[41]	Cat# CCL-221
DLD1-RANGAP1-AID cells (human)	Aksenova et al., 2020[41]	N/A
HEK293 HTv3 cryptic exon reporter cells (human)	this study	N/A
Oligonucleotides		
RNA oligonucleotides	this study	See Table S1
Primers	this study	See Table S2
ON-TARGETplus non-targeting siRNA pool	Dharmacon	Cat# D-001810-10-20
ON-TARGETplus human TARDBP siRNA pool	Dharmacon	Cat# L-012394-00-0010
Recombinant DNA		
pTwist EF1a Puro wtTDP-43-V5	Duan et al., 2022[28]	pK1194
pTwist EF1a Puro TDP-43 5FL-V5	Duan et al., 2022[28]	pK1197
pET 6His-SUMO-TEV-RRM1-2	this study	pK1127
pSLED-TDPv2b	this study	N/A
Software and algorithms		
MetaXpress (v6.1.0.2071)	Molecular Devices	https://www.moleculardevices.com/products/cellular-imaging-systems/acquisition-and-analysis-software/metaxpress#gref
MetaXpress translocation-enhanced and multiwavelength translocation algorithms	Hayes et al., 2020, 2021[28,62]	N/A
MetaXpress nuclear granularity custom module	This study	N/A
Prism (v10.2.1)	Graphpad	https://www.graphpad.com/

(Continued on next page)

Continued

REAGENT or RESOURCE	SOURCE	IDENTIFIER
FIJI/Image J (v2.1.0/1.53c)	NIH	https://imagej.net/software/fiji/
Photoshop 2024 (v25.5.0)	Adobe	https://www.adobe.com/products/photoshop.html

Other

ImageXpress Micro Confocal System	Molecular Devices	N/A
LSM980 Confocal Microscope	Zeiss	N/A
Trans-Blot Turbo Transfer System	Bio-Rad	Cat#1704150
Nano-drop One	Thermo Scientific	N/A
QuantStudio 3 Real-Time PCR System	ThermoFisher	N/A
ImageQuant LAS 4000 System	GE Healthcare	N/A
Spectramax M3 plate reader	Molecular Devices	N/A
UV Stratalinker 1800	Stratagene	N/A

RESOURCE AVAILABILITY

Lead contact

Further information and requests for resources and reagents should be directed to and will be fulfilled by the lead contact, Lindsey Hayes (lhayes@jhmi.edu).

Materials availability

Plasmids and cell lines generated in this study will be shared by the lead contact upon completion of a material transfer agreement.

Data and code availability

- All data reported in this paper will be shared by the lead contact upon request. Original Western blot images are included in the supplement (Figure S5).
- This paper does not report original code.
- Any additional information required to reanalyze the data reported in this paper is available from the lead contact upon request.

EXPERIMENTAL MODEL AND STUDY PARTICIPANT DETAILS

Cell lines

A single cell-derived HeLa cell clone (ATCC; originally female-derived)[61] was maintained in OptiMEM (Gibco/ThermoFisher) with 4% FBS. Monoclonal HeLa cell lines stably expressing V5-tagged wild-type or RRM-mutant TDP-43 were generated by transient transfection using puromycin selection followed by limiting dilution cloning. A monoclonal TDP-43 CRISPR-knockout HeLa cell line was generously provided by Shawn Ferguson[54] and maintained in DMEM (Gibco/ThermoFisher) with 10% FBS. U2OS cells (ATCC; originally female-derived) were maintained in DMEM/F12 with 10% FBS. DLD1-wildtype cells (ATCC; originally male-derived) and DLD1-RanGAP1-AID cells generously provided by Mary Dasso[41] were maintained in DMEM (Gibco/ThermoFisher) with 10% FBS. The HTv3 TDP-43 cryptic exon reporter cell line was generated by stably transfecting HEK293 cells (ATCC; originally female-derived) with the *Adnp2* bichromatic reporter plasmid. Cells positive for mCherry were then sorted by FACS and maintained in DMEM with 10% FBS. All cells were grown at 37° in humidified air containing 5% CO_2, frequently refreshed from frozen stocks validated by STR profiling (ATCC) and verified to be mycoplasma negative (Genlantis).

METHOD DETAILS

Oligonucleotides

Synthetic RNA oligonucleotides were obtained from IDT. Sequences and modifications are listed in Table S1. Desalted lyophilized oligonucleotides were reconstituted in sterile, RNase- and DNase-free water and single-use aliquots were stored at -80°C.

Oligonucleotide transfections

Cells were plated 24 h prior to transfection in optical #1.5 glass- (CellVis: HeLa, U2OS) or plastic-bottom (Ibidi: DLD1, HEK293) 96-well plates at densities targeting 60-70% confluence at the time of transfection. As previously described,[28] synthetic oligonucleotides were transfected using Lipofectamine RNAiMax (ThermoFisher). RNA oligomers were diluted in Opti-MEM and mixed 1:1 with diluted Lipofectamine (1.5-3 µL per 25 µL Opti-MEM). After a 5 min incubation at room temperature, transfection mixes were added to culture media at 10-30 µL transfection

mix per 100 μL media in 96-well plates or scaled proportionally for 6- and 12-well plates for protein and RNA extraction, respectively. The Lipofectamine concentration and volume of transfection complex per well were optimized for each cell line utilizing biotinylated oligonucleotides to maximize dose-dependent nuclear entry, via SAV-647 labeling. The oligonucleotide concentrations shown represent the final concentration following dilution in culture media. Mock transfection controls were treated with Lipofectamine alone. For transcriptional inhibition, cells were treated with 250 nM NVP2 (Tocris, stock in DMSO) for the times indicated in the figure legends. For auxin-induced RanGAP1 ablation, DLD1 cells were treated for 2 h with 0.5 mM 3-indoleacetic acid (Sigma, stock in ethanol). At the time points indicated, cells were fixed in 4% paraformaldehyde/PBS (Electron Microscopy Sciences) for 15 min.

Immunofluorescence

Paraformaldehyde-fixed cells were rinsed once with PBS and then blocked and permeabilized with 10% normal goat serum (NGS, Vector Labs) and 0.1% Triton-X-100 in PBS for 15-30 min at room temperature. Primary antibodies were applied for 1 h at room temperature or overnight at 4°C in 10% NGS/PBS. Following two PBS rinses, AlexaFluor-labeled secondary antibodies (ThermoFisher) were applied for 1 h at room temperature in 5% NGS/PBS. To visualize biotinylated oligomers, streptavidin-AF647 (ThermoFisher) was added together with secondary antibody at 1:500. Cells were rinsed with PBS containing Hoechst 33342 and stored in 50% glycerol/PBS until imaging.

Cryptic exon reporter assays

Reporter constructs were designed based on the TDP-43-regulated cryptic exon found in the mouse gene *Adnp2,* which is flanked by an extended GT repeat. Briefly, the region between exon 2 and exon 3 was PCR amplified from the mouse genome and inserted into a pSLED bichromatic reporter construct as previously described.[63] HEK293 cells were transfected with the reporter plasmid to generate stably transfected cells. Cells positive for mCherry were FACS-sorted to generate the HTv3 cell line. Cells were validated by transfection with scrambled vs. TDP-43 siRNA (Dharmacon) using DharmaFECT 1 according to the manufacturer's instructions. At 48 h, cells were transferred to prewarmed FluoroBrite DMEM (ThermoFisher) supplemented with 10% FBS and Hoechst 33342 for 20 min prior to live imaging. Subsequent oligonucleotide transfections were performed in parallel with siRNA controls as described above.

RNA extraction and RT-PCR

Cells were rinsed in PBS and lysed in RNA lysis buffer (Zymo). Total RNA was isolated using the Quick RNA miniprep kit (Zymo) following the manufacturer's protocol with DNase digestion. cDNA synthesis was performed with the high-capacity cDNA reverse transcription kit (ThermoFisher). RT-PCR for gel electrophoresis was performed using Platinum II Hot-Start Green PCR Master Mix (ThermoFisher), and products separated on 2% EX e-gels containing SYBR Gold II (Invitrogen). qRT-PCR using custom TaqMan primers/probes was performed with TaqMan Fast Advanced Master Mix on a QuantStudio 3 Real-Time PCR System. Prior to cDNA synthesis, samples were spiked with equal volumes of Taqman Universal RNA Spike-In RT control (ThermoFisher) which was utilized as an internal standard. Primer/probe sequences are provided in Table S2.

RRM1,2 cloning and recombinant protein production

The RRM1,2 domain of human TDP-43, including amino acids 102-269, was PCR-amplified from wt-TDP43-tdTomato-HA plasmid (Addgene 28205, a gift from Zuoshang Xu)[64] and cloned in frame with the N-terminal 6-His-SUMO-TEV-site into the SspI site of pET 6His-SUMO-TEV LIC (1S) (Addgene 29659, a gift from Scott Gradia) using the HiFi Assembly kit (NEB). NEBuilder Assembly Tool 2.0 was used to design RRM1,2 primers with 21-bp overlap with the destination vector. The correct sequence of the resulting pET 6His-SUMO-TEV-RRM1,2 plasmid was verified by restriction digests and Sanger sequencing.

6His-SUMO-RRM1,2 protein production was performed in BL21-DE3 *E. coli* cells (Thermo), using LB media with 50μg/ml Kanamycin. Cells transformed with the pET 6His-SUMO-TEV-RRM1,2 plasmid were plated on an LB-agar plate and grown at 37°C overnight. The next day, a 250 mL starter culture was initiated with a single large colony and grown overnight on a shaker at 30°C, reaching OD_{600nm} =∼1.4. 100 mL of the starter was added to 1L media in 2.8L Fehrnbach baffle-free flask and incubated at 30°C, 225 rpm for 3.5 h, reaching OD_{600nm} =∼0.4. The culture was supplemented with 0.3mM IPTG and incubated at 30°C, 100 rpm for 3.5 h before cell harvesting and washing with 10mM imidazole in PBS (pH 7.4), freezing in liquid nitrogen, and storage at -80°C. Protein purification started by quickly thawing the cells in ∼15 mL room-temperature 10mM imidazole in PBS (pH 7.4) with protease inhibitor cocktail (Roche) and freshly added 200μM PMSF. Cells were lysed by sonication on ice and lysates were clarified at 26500g, 40 min, 4°C. The clarified lysate was incubated on a rotator (50 min, 4°C) with 1 mL (packed volume) HIS-Select HF Nickel Affinity Gel (Sigma). The beads were collected in 15 mL Poly-Prep chromatography column (Bio-Rad) and washed with 15 mL 10mM imidazole before stepwise elution with 3mL each of PBS, pH 7.4 containing increasing Imidazole concentrations (25-1000mM). Aliquots of the eluates were separated on a 4-20% SDS-PAGE gel, and peak fractions (corresponding to 50-150mM imidazole) were identified by Coomassie staining. Pooled peak fractions were dialyzed overnight in PBS, clarified at 21000g, 4°C, 3 min, and protein concentration was measured before aliquoting, snap-freezing in liquid nitrogen and storage at -80°C.

EMSAs

Oligonucleotides were diluted to 10 pmol in binding buffer (20 mM HEPES, pH 7.6 containing 25 mM KCl, 1 mM TCEP, and 2 mM $MgCl_2$).[32] A serial dilution of SUMO-RRM1,2 protein (0-40 pmol) was prepared, mixed 1:1 with oligonucleotide, and incubated at room temperature for 1

h. Samples were diluted in 5X TBE running buffer (Invitrogen/ThermoFisher) and run on 10% polyacrylamide gels (Invitrogen/ThermoFisher) at 200 V for 45 min on ice in pre-chilled 1X Ultrapure TBE Buffer (Fisher Scientific). Gels were rinsed in 1X TBE and immersed in SYBR Gold nucleic acid gel stain (1:10,000) (Invitrogen/ThermoFisher) for 30 min prior to fluorescent imaging on an ImageQuant LAS 4000 gel imaging system (GE). Band density was quantified using ImageJ.

Biotinylated RNA-pulldowns

HeLa cells were transfected as described above in 6-well plates and crosslinked for RNA pulldowns as previously described.[28] Briefly, 5 h post-transfection, cells were rinsed with DPBS and UV crosslinked (λ=254 nm, 1.5 J/cm^2 on ice) before harvesting by trypsinization. Cells were washed twice with DPBS, resuspended in lysis buffer (1% NP40 in PBS, pH 7.4 with protease inhibitor cocktail (Roche), and 2.5% v/v RNase inhibitor), and sonicated 10s on ice. After clarification of the lysates by centrifugation (21,000g, 5 min, 4°C) and protein concentration measurement, samples were diluted with lysis buffer to equal concentration (2-4 μg/μL). An equal total protein amount of lysate per sample was then added to DPBS-washed magnetic SAV-conjugated beads (Thermo-Fisher MyOneC1, ~1 μL beads/ 15-20μg sample) and rotated at 4°C for 1.5 h. Beads were collected on a magnetic stand, supernatants removed and beads washed 5 times with ice-cold RIPA buffer (10mM Tris-HCl, pH 8.0, 5mM EDTA,1% Triton X-100, 0.5% Sodium Deoxycholate, 0.1% SDS, 150mM NaCl), transferred to the new set of tubes, rinsed twice with water and resuspended in 20 μL Laemmli sample buffer (Bio-Rad, 2X with 5% β-mercaptoethanol). After boiling for 5 min at 100°C, tubes were briefly centrifuged, placed on a magnetic stand, and the eluates separated by SDS-PAGE, along with aliquots of inputs prepared in Laemmli sample buffer. After transfer to PVDF membranes, immunoblots were blocked for 30-60 min with 5% non-fat dried milk (Biorad) in TTBS (0.05% Tween-20, TBS, pH7.4) and incubated overnight at 4°C with primary antibodies. After incubation with horseradish peroxidase-coupled secondary antibodies (20 min, room temperature) and washes with TTBS, ECL images were photographed using ImageQuant LAS400.

QUANTIFICATION AND STATISTICAL ANALYSIS

Microscopy and automated image analysis

Automated cell imaging was performed on an ImageXpress Micro Confocal high content microscope (Molecular Devices) as previously described.[28,62] Fixed, immunostained cells were imaged with a 20x objective in spinning disc confocal mode with 60 μM pinhole at sub-saturating exposures. A 3 x 3 grid of nine non-overlapping images were routinely collected from each well yielding an average of 1000-3000 cells per well, depending on cell type and density. 96-well plate designs routinely incorporated 2-3 wells per dose or condition to serve as technical replicates, which were combined to generate the mean $\pm$ SD for each biological replicate shown in the figures. Background-corrected mean nuclear and cytoplasmic intensities and the nuclear/cytoplasmic (N/C ratio) were analyzed using the MetaXpress translocation-enhanced module (Molecular Devices). Nuclear TDP-43 granules were analyzed using a custom module set to detect nuclear granules $\geq$ 1 pixel (0.5 μm) in size and $\geq$4000 relative fluorescence units brighter than local background, among non-mitotic cell nuclei. All image analysis was performed on raw, unaltered images and uniformly filtered to exclude errors of cell identification (probe intensity = 0) or non-physiologic results (N/C ratio <0.1 or >100). Live cell imaging of HTv3 reporter cells was done in 20x widefield mode, and dual GFP/mCherry intensities analyzed with the MetaXpress multiwavelength translocation module. High resolution images of oligonucleotide localization and nuclear TDP-43 granules were obtained using a Zeiss LSM980 confocal microscope with a Plan-Apochromat 63x/1.4 oil objective, in confocal and Airyscan mode, respectively. For quantification of TDP-43 nuclear granules in Image J, individual nuclei were outlined, and surrounding pixels discarded ('clear outside' tool). Images were thresholded to the top 5th percentile and the 'analyze particles' tool was used with lower limit $\geq$ 1 pixel (0.035 μm).

Image processing for figures

Minimal processing was done using Adobe Photoshop 2024, limited to cropping and spreading the intensity histogram between the dimmest and brightest pixels in each image. In selected figures, the 'fire' pseudo-color look-up-table (LUT/ImageJ) was applied to aid in data visualization. The LUT is a quantitative and linear map that covers the full range of the data. All adjustments were linear (no gamma changes) and applied equally to the entire image. Immunoblots and gels were cropped for space and the intensity histogram was spread between the dimmest and brightest pixels. Unmodified gel images are shown in Figure S5.

Statistical analysis

Curve fitting and statistical analyses were performed using Prism software (Graphpad). Dose-response curves were fit by simple linear or non-linear regression analysis. Differences among groups were analyzed by ANOVA with post-hoc tests for multiple comparisons as detailed in the figure legends. Statistical significance is denoted as follows: ns (not significant), *p<0.05, **p<0.01, ***p<0.001, ****p<0.0001. The number of biological replicates (independent cell passages and experiments) was used as the N for all analyses, unless otherwise noted in the figure legend. Outliers were detected with the Grubbs (extreme Studentized deviate) method to detect a single outlier (α = 0.05). This resulted in one outlier being removed (Figure 6D).